

From pilot site knowledge via integrated reservoir characterization to utilization perspectives of a deep geothermal reservoir: 3D geological model at the research platform Groß Schönebeck in the Northeast German Basin

Ben Norden (✉ Ben.norden@gfz-potsdam.de)

German Research Centre for Geosciences <https://orcid.org/0000-0003-2228-9979>

Klaus Bauer

GFZ German Research Centre for Geosciences, Telegrafenberg, 14473 Potsdam, Germany

Charlotte M. Krawczyk

GFZ German Research Centre for Geosciences, Telegrafenberg, 14473 Potsdam, Germany. TU Berlin, Institute for Applied Geosciences, Ernst-Reuter-Platz 1, 10587 Berlin, Germany

Research

Keywords: Groß Schönebeck, 3D geological modelling, petrophysical parameterization, site development, Permian, Elbe reservoir, Permo-Carboniferous volcanic rocks

Posted Date: June 9th, 2022

DOI: <https://doi.org/10.21203/rs.3.rs-1660889/v1>

License:  This work is licensed under a Creative Commons Attribution 4.0 International License. [Read Full License](#)

Version of Record: A version of this preprint was published at Geothermal Energy on January 6th, 2023. See the published version at <https://doi.org/10.1186/s40517-022-00242-2>.

Abstract

The Groß Schönebeck site in the North German Basin serves as research platform for studying the geothermal potential of deeply buried Permian reservoir rocks and the technical feasibility to extract their geothermal heat. The structural setting of the site was investigated in more detail by studying a newly acquired 3D-seismic survey to improve the structural picture that was based on several old 2D seismic lines so far. The new data allows a revision of the geological interpretation of the site, enabling the set-up of a new reservoir model and providing base information for a possible further site development of the Permian and Permo-Carboniferous targets. The 3D seismic of Groß Schönebeck allows for the first time a consistent geological interpretation and model parameterization of the well-studied geothermal site. Main reflector horizons and the corresponding stratigraphic units were mapped and the structural pattern of the subsurface presented in the 8 km x 8 km x 4 km large seismic volume. While some fracture and fault patterns are visible in the upper Zechstein and post-Permian units, formerly hypothesized large offset faults are not present in the Rotliegend reservoir itself. However, a well-established graben-like structure at the top of the Zechstein succession is most likely related to broken anhydritic Zechstein stringers. Most reflectors above the salt show a rather undisturbed pattern. The main reservoir sandstone of the Dethlingen Formation (Rotliegend) was mapped and characterized. The base of the underlying Permo-Carboniferous volcanic rock sequence and hence its thickness could not be depicted reliably from the geophysical data. Based on the new seismic data and the available reconnaissance drilling, logging, and laboratory data of the Groß Schönebeck research site, the thickness and distribution of the sedimentary Rotliegend (with emphasis of the sandy reservoir section) and of the volcanic rock sequence was modelled and parameterized with petrophysical properties (i.e., total and effective porosity, fluid permeability, bulk density, thermal conductivity, thermal diffusivity, and specific heat capacity), providing a more realistic reservoir description. The data and interpretation constitute the basis for a better understanding of the dominating processes at the site and for future measures. Further site development could include a deepening of one well to give evidence on the volcanic rock sequence and consider deviated wells into favourable zones and the design of a fracture-dominated utilization approach.

Introduction

The planning of the overall exploitation concept for low-enthalpy geothermal resources strongly depends on both regional and local geology and includes the drill path design (directional drilling, deviation) and stimulation operations in case of low-productive reservoirs (e.g., von Hartmann et al., 2015; Kana et al., 2015; Ricard et al., 2016). For the development of an adequate (site-specific) exploitation strategy, knowledge on the existence and orientation of large-scale faults, fracture networks and of a possible compartmentalization of target horizons are of utmost importance (c.f., Buness et al., 2014; Krawczyk et al., 2015). Imaging these structural features at depth and including this knowledge in reservoir models greatly expands the basis for an efficient use of geothermal energy (e.g., Bauer et al., 2010; McGuire et al., 2015).

Among the sedimentary basins worldwide that contain deep geothermal resources (Mendrinis et al., 2010; Pussak et al., 2014; Siler et al., 2016; Zhang & Hu, 2018), the North German Basin is one of the three type locations in Germany that offers potential for geothermal heat production. At the Groß Schönebeck research platform, reconnaissance boreholes and vintage 2D seismic lines were lately supplemented by 3D reflection seismic (Krawczyk et al., 2019) and VSP (Henniges et al., 2021) surveys, which provide the basis of the new geological and reservoir model presented in this manuscript.

We address here the development of a new site model for the Groß Schönebeck geothermal research platform, that shows along the example of Groß Schönebeck how already existing knowledge and adapted procedures can help developing a site for geothermal use. For the North German Basin type lithologies, we expand here covering Carboniferous to Cenozoic units and provide reservoir model parameterization of the Permo-Carboniferous target zones that are important for future deep geothermal development. The knowledge and the data sets gained at Groß Schönebeck will also help planning exploitation concepts for similar geological settings.

Geological Setting

The Groß Schönebeck deep geothermal research platform is located in the Northeast German Basin (NEGB) which is part of the Central European Basin System reaching from Middle England to North Germany, Poland and the Baltic States (Fig. 1, Ziegler, 1990; Doornenbal and Stevenson, 2010), reflecting a low-enthalpy geothermal setting. The basin developed in the late Carboniferous and early Permian in response to thermal relaxation, crustal extension and tectonic subsidence (van Wees et al., 2000). The subsequent sedimentation resulted in the deposition of sedimentary rocks with a thickness of up to 6.500 m in the NEGB (Hoth et al., 1993; DEKORP-BASIN Research Group, 1999). The NEGB was like other sub basins of the Permian Basin System a target area for the hydrocarbon industry. Several seismic campaigns and deep drillings were performed to investigate the expected most prospective target zones, like the Permian Rotliegend sediments, also in northeast Brandenburg (Fig. 1). The geological evolution of the basin and its lithological composition will be summarized shortly in the following.

Pre-Permian Basement and Permo-Carboniferous volcanic rocks

In the study area (Fig. 1), details on the Carboniferous and pre-Carboniferous basement are not well constrained. Devonian rocks are proven to be partly absent in the sedimentary succession (Belka et al., 2010) and are indeed not drilled by any deep borehole in Brandenburg (Franke, 2015a), although they may be expected in depths of more than 6–7 km. Maximum drilled depths to about 5.2 km give evidence of Lower Carboniferous (Dinantian) rocks in Brandenburg. The rocks encountered consist of fine-grained to coarse-grained greywacke, siltstones and pelites of a distal to proximal flysch facies type (Kopp et al., 2004; Kombrink et al., 2010; Franke, 2015b). These deposits of the Carboniferous “Kulm” facies are characterized by a variable dipping of 0–90° and are strongly fissured due to the Variscan orogeny (the Visean of the E Ob 1/68 borehole, Fig. 1). During Permo-Carboniferous times, Brandenburg was part of a back-arc extension regime of the Variscan foreland. In the Westphalian, there was in contrast to the coal-bearing deposits of large areas of Northwest Europe, non-sedimentation in the study area (Kombrink et al., 2010). Due to the progressing thermal subsidence of the evolving extensional regime, the Permian Basin System developed. As a first consequence, an intense volcanic activity resulted in thick successions of Permo-Carboniferous volcanic rocks (Fig. 1). These volcanic sequences do often represent a kind of magmatic basement filling of the sedimentary NEGB. According to Breitzkreuz & Geißler (2015),

Mg-andesitic rocks dominate in the East Brandenburg Sub Province (Geißler et al., 2008). About 48 boreholes encountered the volcanic succession, but only 10 drilled the volcanic complex completely in East Brandenburg. As described by Benek et al. (1996) and Geißler et al. (2008), the Permo-Carboniferous volcanic succession is characterized by different mineralogical composition and variable rock texture according to the magma, eruptive type and stage, whereby two of five eruptive stages are present in East Brandenburg. The oldest volcanic rock units of the first eruption stage consist of dacitic rocks, followed by lower basaltic andesitic rocks, rhyolitic rocks and middle and upper basaltic andesitic rock units. In East Brandenburg the volcanic succession ends with trachytic rocks of the early phase of the second eruption stage in the lowermost Asselian (Benek et al., 1996). The andesitic rocks do predominate the entire succession and built up to 80% of the total volcanic rock (Huebscher, 1995). The andesites are commonly porphyritic consisting of plagioclase, orthopyroxene and olivine (Benek et al., 1996). According to Benek et al. (1996) the entire andesite complex averages a thickness of 200–500 m with a local maximum thickness of more than 1000 m at shield volcanos (E Ob 1/68 well, Fig. 1). Based on their analysis, an initial thickness of about 200 m could be expected for the Groß Schönebeck area.

Middle European Permian (Dyas)

Sedimentary Rotliegend

During the Permian, the subsidence of the NEGB causes the deposition of large volumes of sedimentary rocks. In Brandenburg, the primary source rocks of these Rotliegend sediments were the thick andesitic rock sequences. Carboniferous rocks were, although often separated by an unconformity from the Rotliegend sediments, not supply rocks of the deposits (Rieke, 2001). The high altitude areas of the volcanoes were eroded and deposited in braided plain and aeolian to fluvial environments at the basin margin and in sand flat and mud flat environments at the distal areas of the basin centre. Different subsequent climatic and tectonic events trigger basin-wide traceable sedimentary cycles in the Rotliegend with sequences of thicknesses of 20–100 m (Rieke et al., 2003). The cycles often start with clay/mud-dominated horizons (highstand) and evolve to more regressive sediments (shoreface and deltaic sands toward the top which progrades laterally into offshore shales, lowstand) and end with the next maximum flooding surface (highstand; Gast 1995). According to Gebhardt et al. (1991), tectonic events are the main cause for the development of the fining-upward cycles of the Parchim, Mirow, Dethlingen und Hannover Formations. The climatic conditions during the Rotliegend were semi-arid to arid, causing the dominating Fe-oxidized reddish colour of the deposits.

The area of Groß Schönebeck is situated in a SE marginal position of the NEGB. Here, clast supported coarse-grained conglomerates and sandstones of the Havel Subgroup cover the Permo-Carboniferous volcanic rocks (E GrSk 3/90 borehole, Figs. 1 and 2). Holl et al. (2005) interpreted these deposits as fluvial sediments of coarse-grained bedload rivers in a braided plain environment. In the E GrSk 3/90 borehole, the multistoried channels were deposited in a NNE to NW striking depositional system with a mean palaeocurrent direction of 24° for the Lower Havel Subgroup and 340° (NW) for the Upper Havel Subgroup (Holl et al., 2005). By the end of the Havel Formation, the landform configuration changed fundamental. Due to thermal subsidence, the North-German trough extended further to the west reaching the Netherlands and England (Gast and Gebhardt, 1995). The rise of the hinterland allows the development of erosive sandy deposits which cover the entire southern margin of the NEGB. These quartz-dominated sandy deposits represent one of the geothermal reservoir target, the Elbe reservoir sandstone (ERS) that is equivalent to the so-called *Elbebasissandstein* (EBS) of Bauer et al., 2020.

The ERS is well documented in boreholes along the marginal areas of the NEGB (Fig. 2 and Gast et al. 1998; McCann 1998). Stratigraphically, the ERS comprises parts of the Dethlingen Formation, the Hannover Formation, and possible parts of the Mirow Formation (Fig. 2). The ERS shows a variable thickness of up to about 200 m near the coastline (Lindert et al., 1990) and thins out towards the basin centre. Many samples of the ERS show a bimodal grain-size distribution. Plein (1995) interprets the sandstone to represent sand that was accumulated under aeolian conditions of the hinterland first before it was transported by aquatic processes toward the basin and lithified. In the E GrSk 3/90 well, the ERS shows a thickness of about 40 m within the Dethlingen Formation (Bauer et al., 2020, sandstone interval with low GR intensity in Fig. 2). According to Holl et al. (2005), the fine- to coarse-grained sandstones were deposited in an ephemeral stream floodplain environment. The palaeocurrent direction distribution is more variable as in the Havel Subgroup but is still to the NW (mean azimuth: 290°; Holl et al., 2005). In open-hole logs, the ERS is characterized by low gamma-ray values and shows a high quartz content. In addition, decreased P-wave velocities observed by sonic logging indicate an increase of porosity (Trautwein and Huenges 2005). These two observations explain the general interest in the ERS as a geothermal target, hosting water of about 150°C temperature in Groß Schönebeck (Huenges, 2002).

Within Rotliegend times, the sedimentation regime in the central area of the basin got more and more influenced by cyclic fluctuations of the water table, and a growing salt lake developed from the central part of the basin (Gast and Gebhardt, 1995). A progressive planation of the morphology in combination with the reduction of sediment supply resulted in the development of sediments of the mud flat facies. The playa deposits cover large parts of the NEGB during the late Rotliegend (Rieke et al., 2001; Gast et al., 2010). This is also the case in Groß Schönebeck, where mudstones do predominate the lithology of the Hannover Formation, partly interrupted by sandy deposits of a sandy mudflat environment.

Zechstein

During the Late Permian, the basin developed to an intracontinental topographic depression which was rapidly flooded by a catastrophic transgression from the Barents Sea (Peryt et al., 2010, Strozyk et al., 2017). In many areas, the uppermost 10–15 m of Rotliegend sandy sediments were reworked and form the Weissliegend which locally grades into limestone and is overlain by the Kupferschiefer (Peryt et al. 2010). Subsequently, cyclic occurring flooding events lead to the deposition of 1500–2000 m of Zechstein deposits reflecting progressive evaporation (e.g., Zhang et al., 2013). The cyclicity is represented by the Zechstein deposits consisting of transgressional carbonates and mudstones followed by evaporates (Peryt et al., 2010). The nowadays thickness of Zechstein deposits is very variable and triggered by post-Permian salt movement (salt tectonics) and erosion (see later in text). In Groß Schönebeck, which is located on top of a salt pillow, the Zechstein sequence shows a total thickness of approximately 1500 m.

Post-Permian deposition and evolution of salt structures

In the late Permian, a phase of accelerated subsidence commenced as a result of thermal contraction and continued until the end of the early Triassic in the NEGB. Since then, subsidence rates were decreasing exponentially according to a thermal subsidence pattern (Scheck et al., 1999). Only for time intervals in the late Triassic as well as the late Cretaceous and Cenozoic, the subsidence rates were accelerated again, varying spatially in magnitude within the basin (Scheck et al., 1999; Kossow & Krawczyk, 2002). In the mid- to late Triassic, the thinning of supra-salt sediments due to an extensional regime in conjunction with subsidence caused instabilities of the Zechstein salt deposits and initiated the formation of salt structures (Kossow et al., 2000; Scheck et al., 2008). In the late Cretaceous to earliest Cenozoic, salt diapirism was associated with compression (Scheck et al., 2003). After this compressive phase, the Cenozoic subsidence phase enabled further intensive salt movement. In relevant areas, Pleistocene glaciations may have triggered still active salt movements due to the loading and unloading of ice sheets (Strozyk et al., 2017).

German Triassic (Buntsandstein, Muschelkalk, Keuper)

The deposits of the *Buntsandstein* form the first sediments above the Zechstein. Still arid conditions with fluvial sedimentation did prevail in that time (Stackebrand and Röhl, 2015). Only the Middle Buntsandstein shows higher depositional energies resulting in a higher and coarser-grained sand content while the Lower and Upper Buntsandstein consists of clayey to fine-grained sediments. The coarser-grained sandy deposits within the Volpriehausen, Dethfurt, Hardegsen, and Solling Fms. (Middle Buntsandstein) are often discussed as possible geothermal reservoirs. At Groß Schönebeck, the thickest sandstone interval occurs in the Dethfurt Fm. with a thickness of 10 m, showing a cleaner sand interval of about 6 m and temperatures of 85°C at a depth of 1870 m. The ingress of marine conditions in the Upper Buntsandstein and the forming of evaporates resulted in basin-wide traceable impedance contrasts in the lithological succession and in prominent seismic markers (S1 and S2, Fig. 3).

In the *Muschelkalk*, the NEGB was connected in the south with the Tethys Ocean and formed an epicontinental flat sea. Calcareous sediments like marlstones and limestones do represent the predominant lithotypes of this time. The Muschelkalk is divided in three subunits (Lower, Middle, and Upper). In the Lower Muschelkalk, oolitic limestones of the so-called Wellenkalk could represent a potential geothermal reservoir if fractured and appropriate fluid paths are present. In Groß Schönebeck, the E GrSk 3/90 borehole did not observe any fluid flow in this succession during drilling. Measured temperatures amount to 70°C in the respective depth interval (1500–1550 m). In the Middle Muschelkalk, the connection to the Tethys was sporadically closed, resulting in the formation of evaporitic sediments. Basin-wide traceable seismic marker horizons are connected to this event (M1 and M2, Fig. 3).

The *Keuper* represents the Upper German Triassic. Keuper sediments are predominantly represented by fine-grained deposits of the stillwater facies, of fluvial facies, and subordinate of marine facies. Based on basin-wide recognizable discontinuities, the Keuper is subdivided in several formations (Fig. 3, e.g., Beutler and Franz, 2015). Depending on the respective lithological composition and succession, the discontinuities are partly related to more or less pronounced seismic reflectors (K1, K2, Fig. 3). According to Beutler and Franz (2015), the unconformity forming the boundary of the Grabfeld Formation and the Stuttgart Formation was related to tectonic events which also causes the first salt diapir forming phase. The salt structure of Groß Schönebeck formed during Keuper times and represents a salt pillow with only minor hiatus of less than 30 m (Beutler and Franz, 2015).

Jurassic, Cretaceous and Cenozoic

The movement of salt during the Upper Triassic causes the formation of troughs and highs and affects post-Triassic sedimentation and erosion processes. For Groß Schönebeck, only Lower Jurassic (Northern Lias Group) sediments are present in the drillings on the salt pillow (Fig. 4). The deposits represent marine shale facies and are partly interfingering with shallow-marine sands and limnic and terrestrial sediments. The change of lithological composition due to different facies conditions allow the mapping of several seismic horizons with variable reflectivity (L2 and L4, Fig. 4).

During most of Lower Cretaceous times, almost the complete area of East Brandenburg was part of a structural high without any preserved sediments. At the upper Lower Cretaceous, the highland of East Brandenburg became part of a marine depositional environment, which continued to the Upper Cretaceous. Depending on the particular structural situation (paleogeography), respective sediments were deposited (e.g. E GrSk 2/76, Fig. 4).

In the Tertiary, large parts of the NEGB became flooded. Marine clayey sediments of the Oligocene (the Rupelian "Rupelton") document the basin-wide marine transgression of the paleo-North Sea. In salt rim synclines, the Tertiary could achieve a much greater thickness (see E GrSk 3/76, Fig. 4). Changing water tables and coastline conditions in the Miocene allow the formation of coal beds (lignite) in southeast Brandenburg. In the late Tertiary (Middle Miocene to Pliocene), the marine conditions in Brandenburg vanished owing to another regression. Therefore, sediments of that age are almost not present in northeast Brandenburg.

The Quaternary deposits are dominated by glacial sediments of the different ice ages (boulder, sand, clay, till, Fig. 4). They host the main fresh water resources. Due to glacial troughs that cut into the underlying strata and allow the deposition of glacial sediments, the Quaternary thickness could vary significantly on short distances.

Data And Methods

The presented study included various types of subsurface data, covering different scales and different qualities which are shortly addressed in the following.

Literature and map data. For regional correlation, the geological atlas of Brandenburg (Stackebrand and Manhenke, 2010), providing different thickness and depth maps of units of the Mesozoic and Cenozoic was helpful. In parts, former synopsis representations of legacy exploration data could be used (e.g., Lange et al., 1981; Doornbal & Stevenson, 2010).

Borehole data. Mainly due to the efforts of the hydrocarbon exploration in the time period of 1960–1990, several deep drillings provide valuable underground information and are available for cross-correlation (Hoth et al., 1993). In the Groß Schönebeck area, the E GrSk 2/68 borehole, the E GrSk 3/90 borehole, which was deepened in 2001 as a geothermal well, and the Gt GrSk 4/05 geothermal well provide unique access to underground data (Fig. 1, Table 1). Of special interest are the geophysical logging data, still available cores (E GrSk 3/90), the respective drilling reports, and petrophysical studies (e.g., Trautwein, 2005;

Trautwein and Huenges, 2005; Blöcher et al., 2016) for correlation and petrophysical interpretation and parameterization of the model. The former studies for Groß Schönebeck focused on the Permo-Carboniferous reservoir targets and disregard most of the available post-Rotliegend drilling and borehole data.

By using the well data it became soon obvious, that the data of the E GrSk 3/90 borehole and especially of the Gt GrSk 4/05 borehole need to be reinterpreted based on a consistent depth reference log covering the complete drilled sequence. This enabled a consistent interpretation of the drilled lithological and stratigraphical units for the two close-by boreholes. In the E GrSk 3/90, an electrical image log was measured in the Rotliegend reservoir section. This was used for an analysis of depositional structures (Holl et al., 2005). Based on the work of Holl et al. (2005), an analysis of the sedimentary dip azimuths using the azimuth-vector plot method (after Rider, 2000) was applied. Here, dip azimuth values are plotted sequentially in their true orientation but without any depth scale. Dip azimuth changes due to different sedimentary regimes will result in different line orientation. For petrophysical interpretation, gas-derived laboratory permeabilities were corrected using the approach of Juhasz (1986), and permeability was additionally calculated using available log data based on the approach of Coates et al. (1991):

$$k = a \cdot \Phi^b \cdot \left(\frac{F}{B}\right)^c$$

1

where k is permeability, Φ is total porosity, B is bound fluid volume (calculated as the product of the volume of clay, V_{Cl} , and the clay total porosity, Φ_{Cl}), F represents the free fluid volume ($F = \Phi - B$), and a , b , c are empirically derived constants. The Coates equation is fitted to laboratory data by adjusting the constants a , b , and c .

Seismic data. The main input for the structural geological model represents the newly acquired 3D seismic of Groß Schönebeck. For main acquisition and processing parameters of this survey see Krawczyk et al. (2019). For well-tie integration, data from a vertical seismic profile conducted in the E GrSk 3/90 and Gt GrSk 4/05 boreholes with a distributed acoustic sensing system (Henniges et al., 2021) provided important input. The study of Bauer et al. (2020) to decipher a seismic facies classification on the Rotliegend sandstone reservoir was used to enhance the structural modelling and petrophysical property simulation for the *EBS*. In addition, former legacy 2D seismic surveys in the study area of the 3D seismic were available in a digital format or as georeferenced scanned images.

Hydraulic data. The Permian Rotliegend Elbebasissandstein and the succession of the drilled volcanic rocks were stimulated hydraulically in Groß Schönebeck. Respective data (Blöcher et al., 2016) provide information on the in-situ hydraulic and mechanical behaviour and the stress regime of the Permian reservoir zones. During stimulation, passive seismic sensing was applied. The recorded microseismic events (Kwiatek et al., 2010) and their in-depth interpretation (Blöcher et al., 2018) provide further information on the reservoir setting and model parameterization.

Table 1

Data used for the new geological model of Groß Schönebeck. For location of boreholes see Fig. 1. Abbreviations of different processed seismic volumes: PoSTM – post-stack time migration, NMO – normal move out, PreSDM – pre-stack depth migration, DeMultiple – suppression of seismic multiples.

Kind of data	Name(s)	References
Boreholes – stratigraphy and main lithology	E Ob 1/68, E GrSk 2/67, E GrSk 3/90, Gt GrSk 4/05	Hoth et al., 1993; Holl et al., 2005
Boreholes – petrophysical rock analysis (cores)	E GrSk 3/90	Blöcher et al., 2016; Trautwein, 2005
Boreholes – geophysical well logging	E GrSk 3/90, Gt GrSk 4/05	Huenges & Hurter, 2002
2D seismic of Finowfurt and Eberswalde campaign	FIW LEW	unpublished data
3D seismic of Groß Schönebeck	PoSTM, NMO Stack, CRS-Stack, CRS-PoSTM, PreSDM-DeMultiple (in time and depth domain)	Krawczyk et al., 2019, this paper.

The available types of underground data were interpreted using the commercial interpretation software Petrel 2016, which was also partly used for seismic analysis, seismic-well tie, horizon interpretation, model building, facies simulation, and petrophysical modelling. Seismic attribute analysis and visualization techniques were performed in time and depth-domain volumes using the Petrel 2016 software package.

Summary of operational site development at Groß-Schönebeck

The research platform Groß Schönebeck is located 40 km north of Berlin and was established over the last two decades. The target horizons for geothermal utilization were Permian and Permo-Carboniferous rocks, hosting in-situ temperatures of about 150°C. The site development started with the re-opening of a non-successful 4.2-km-deep hydrocarbon exploration well in 2001 (the E GrSk 3/90 well, which was drilled in 1990) and was followed by initial hydraulic tests and the drilling of a new geothermal research well (the Gt GrSk 4/05 borehole, completed in 2006 as production well). Hydraulic stimulations were performed to increase the fluid inflow to the Gt GrSk 4/05 borehole. Further tests including the installation and operation of a geothermal loop followed. The pumping of the high-saline reservoir fluids successively depicted obstacles which hindered a lasting operation of the geothermal loop and thus the commissioning of a heat conversion plant (see summary in Blöcher et al., 2016).

So far, the geothermal exploitation concept relied on a matrix-dominated approach, and sparsely distributed 2D seismic profiles (acquired from 1971 and 1999) were used to set up a first 3D geological model of the Groß Schönebeck area, forming the base of the first exploitation concept and the well design of the Gt GrSk 4/05 borehole (Moeck et al., 2009). To conclude, the experiences made with this concept were not successful. As an alternative, a concept based on an engineered fracture-dominated exploitation approach for establishing a continuous and sustainable geothermal loop came into discussion. In order to exclude any structural obstacles, a 3D seismic exploration campaign was performed to shed light into the detailed structural setting of the site. Thereby, Krawczyk et al. (2019) identified the first time determinants for further field development at the site: formerly hypothesized crustal-scale faults, indications for free gas, seismic compartmentalization in the sub-salinar, and a fracture-dominated Rotliegend reservoir were all not proven. Rather, the seismic facies diversity of the reservoir target units (Bauer et al., 2020) leads to the interpretation of a system of thicker paleo-channels deposited within a deepened landscape.

These findings may influence the geothermal exploitation concept, so that we present here an in-depth reservoir investigation of the structural setting, including the interpretation of seismic horizons and involved fault systems.

Seismic-well tie and horizon mapping

Seismic-well ties rely on the available logging data and horizon interpretations. For the Groß-Schönebeck data, in a first step, composite gamma density and sonic velocity logs were compiled for the depth range of the E GrSk 3/90 borehole (Fig. 5). Because sonic velocity and gamma density were not measured above 2332 m and 3850 m, respectively, this composite log contains logging data from neighbouring wells covering the same stratigraphy and similar lithology and, additionally, for uncovered sections estimated density values. The resulting composite logs should represent at least a realistic sonic/density-distribution scenario for the entire drilled sequence. Additional velocity data was acquired with the DAS technique and provides a direct and robust time-depth relation that was used to calibrate the compositional sonic log. This data is available from a depth of 815 m to ca. 4250 m, covering one-way travel time and respective (measured and true vertical) depth information with a spacing of 25 m. Based on the calibrated sonic data, a synthetic seismogram was modelled to support the horizon interpretation of the 3D seismic PoSTM data. The depth-converted PreSDM-DeMultiple volume was processed by a company to remove reflection horizon multiples especially for the sub-salt depth domain. Horizons interpreted in that volume were later shifted to the respective horizon depth encountered in the boreholes.

The complete suite of seismic horizons and their interpretation in the seismic volume is given in Table 2. The uppermost seismic reflector, which is traceable in the seismic volume, represents the L2 reflector. Reflectors above are fragmentary and hard to follow in the seismic volume. Dominant, continuously developed reflectors are the L2, L4, M2, S1, S2, X1, X2 (X3), and the Z(1–3) reflectors (c.f., Krawczyk et al., 2019). Less pronounced are the reflectors K2, K3, M1, M3, R2, and R6(H6). A distinct reflectivity related to the base of the volcanic rocks (R8/C1) was not observed in the volume.

Table 2
Seismic horizons mapped in the new Groß-Schönebeck 3D seismic data set, calibrated with borehole data. Reflector names are according to Reinhardt (1993).

Reflector	Horizon	Reflector quality	Stratigraphy
B2	near base of Upper Cretaceous	weak (uncertain)	CRETA-CEOUS
BLC	near base of Lower Cretaceous	weak	
L2	within Jurassic (Pliensbachian)	variable	JURASSIC
L4	near base of Lower Jurassic	strong	<i>Lias</i>
K2	near top of Weser Formation	variable (uncertain)	TRIASSIC
K3	near top of Grabfeld Formation	well developed	<i>Keuper</i>
M1	near top of Middle Muschelkalk	strong	TRIASSIC
M2	within Middle Muschelkalk (anhydrite)	well developed	<i>Muschelkalk</i>
M3	near base of Mittlerer Muschelkalk	strong	
S1	within Röt Formation (top of anhydrite)	strong	TRIASSIC
S2	near base of Röt Formation	strong	<i>Buntsandst.</i>
X1	near top of Zechstein	strong	PERMIAN
X3	near basal anhydrite (Leine Formation)	strong	<i>Zechstein</i>
	near top of basal anhydrite (Staßfurt Fm.)	Very strong	
Z3	near base of Zechstein	well developed	
R3	within Dethlingen Formation	variable (uncertain)	PERMIAN
Top ERS	near top of Elbe reservoir sandstone	variable (uncertain)	<i>Rotliegend</i>
Base ERS	near base of Elbe reservoir sandstone	well developed	
R6	near base of sedimentary Rotliegend	well developed	
R8	near base of volcanic succession	very weak (uncertain)	PERMO-CARBONIF.

Structural and lithological interpretation

The focus of the 3D seismic survey aimed at the exploration of the Rotliegend (pre-Zechstein; Krawczyk et al., 2019), so that the seismic survey was optimized for imaging deep targets which results in a lower coverage of the shallower subsurface. The most dominant seismic feature within the data is the Zechstein salt structure. While the sedimentary Rotliegend and the top of the Permo-Carboniferous volcanic rocks were also imaged by the seismic data, deeper Pre-Permian structures are hard to elaborate, the more since related borehole data is absent. Figure 6 shows for one section of the seismic volume the challenges associated with the geological interpretation at salt structures. The seismic processing applied and its visualization affects the overall appearance of reflector continuity and intensity. To improve the correct location of reflection surfaces, the CRS-stack based seismic reflection imaging is providing information that is more reliable (Fig. 6B and 6C vs. 6A). Due to strong velocity contrasts and changes by the salt doming, the corrections are highly relevant. Reflection multiples of shallower surfaces may also overlay deeper (and weaker) reflections. Processing of the seismic volume by calculation of the behaviour of reflector multiple of main shallow reflectors and subtracting them from the deeper parts of the volume may allow a more precise interpretation (Fig. 6C). However, the complexity of the processing procedure may also introduce (artificial) artefacts like at the edges of the volume and for the trace-like feature visible in Fig. 6B and 6C.

Pre-Permian and Permo-Carboniferous volcanic rocks

Some local structures and internal features within the pre-Permian are present but hard to relate to a more specific geological interpretation (Fig. 7). The volcanic rocks encountered in the E GrSk 3/90 and Gt GrSk 4/05 boreholes are not well characterized by the seismic volume. Changes in thickness of the volcanic succession or in its chemical composition is not resolved by the seismic data. In profile B and C (Fig. 7), there is an area of increased reflectivity visible in a zone about 1 km east of the GrSk drill site. Remarkably, the profile B shows in that zone a dominant feature with changing polarities (black arrow), probably related to a heterogeneous lithology, a fractured or tilted structures of the Carboniferous or even to processing artefacts rather than reflecting gas-bearing units. Based on the seismic data, at least two scenarios for the base of the volcanic sequence (the top of Carboniferous) are possible. At the supposed top of Carboniferous in the E GrSk 3/90 borehole, a weak seismic reflector is more or less traceable in the seismic volume (the upper C1? indication in Fig. 7). However, the lithostratigraphical boundary was indirectly deduced by well-log interpretation, only (Holl et al., 2015), and the interpretation is still under debate. There is a second reflectivity in a depth range of about 4400 m that is often recognizable in the seismic volume. The reflector is beyond well control but could represent an internal reflector within the Carboniferous, or even correspond to a reflectivity related to the top Carboniferous. We mapped both: one referring to a volcanic sequence thickness of about 70 m (Fig. 8A) and another referring to the lower C1 reflector shown in Fig. 7, referring to a thickness of more than 200 m (Fig. 8B).

Permian

While the petrothermal target of the Permo-Carboniferous volcanic rock succession is not very well resolved by the seismic data, the base of the sedimentary Rotliegend, corresponding to the base of the Havel Subgroup for the area of the seismic survey, is related to a seismic reflector in a depth of about 4140 m that is named R6. The R6 reflector (Table 2 and Fig. 7) marks the transition of well-cemented conglomeratic deposits of the Havel Subgroups to the volcanic extrusive rocks and is related often to a zero crossing from negative to positive amplitude change (from lower to higher velocities).

Above the R6 reflector, the *ERS* represents a well traceable unit with lower seismic velocities, represented by lower amplitudes at the transition from the more porous sandstone to the conglomeratic but more dense Havel Subgroup in Fig. 7. Due to the low thickness of the ERS, the true thickness distribution could not be resolved from the seismic data directly. Therefore, we used the analysis of Bauer et al. (2020) to constrain its thickness better. Based on the seismic-well tie (Fig. 5), we picked the expected top and base of the ERS from the seismic data. Due to the thickness range, which is close to the seismic resolution for the corresponding depth, the mapped reflectors will not give a precise position of the depth interval of this lithological unit except for the wellsite locations where we have direct information. Especially in the NW part of the volume, the top of ERS is hard to follow. To implement the results of the seismic facies analysis (Bauer et al., 2020) in the geological interpretation, we construct a theoretical medium positioning of the ERS (using the average depth of the mapped seismic reflectors of top ERS and base ERS) first. Then, trend maps of the thickness distribution from Bauer et al. (2020) together with the picked horizons and the borehole data were used to model a more representative thickness distribution of the ERS within the seismic volume.

Another reflector in the sedimentary Rotliegend is picked as *R3* reflector. It is interpreted as the top of the more sandy deposits of the Dethlingen Formation and may correlate to near of the base of Eldena (Fig. 2). The silty to clayey deposits of the Hannover Formation and uppermost Dethlingen Formation above the R3 show often horizontal and less pronounced reflectors (Fig. 7).

Faults within the sedimentary Rotliegend are not traceable along several seismic lines. There are some indications for possibly subseismic faults in certain lines but they vanish on a very small scale. Attribute analyses for the base of ERS and other horizons (like R3 or R6) do not show any distinct fault pattern.

The sedimentary Rotliegend shows a smooth trend of lower depths in the northeast (about 4095 m) compared to the southwest (around 4185 m). The total thickness from the base of the Havel Subgroup (R6) to the base of the Zechstein succession (Z3) is increasing from NE to SW from about 300 to close to 400 m in the southern margin of the seismic volume with a mean thickness of 345 m (Fig. 8B).

The Zechstein deposits represent a succession of rocks with different density and sonic velocity, for instance of salt and anhydrite or salt and limestone. The resulting strong impedance contrasts are providing strong and distinct seismic reflectors in this formation. Due to the basin-wide cyclicity of the Zechstein deposits, these seismic markers are also traceable basin-wide on seismic sections. The base of Zechstein (Z3, Figs. 5–7) is seismically very well developed because the anhydrite-mudstone transition from Zechstein to the Upper Rotliegend has a strong acoustic impedance contrast. It is located at a depth of ca. 3750–3800 m. In the E GrSk 3/90 borehole, the base of the Zechstein succession (the Werra Formation) consists of a 30-cm thick black mudstone, representing the “Kupferschiefer”, 5 meters of limestones and marlstones, and 67 m of anhydrite (intercalated with anhydritic halite). Above the Werra Formation, representing the first Zechstein cycle, the basal Staßfurt Formation (2nd Zechstein cycle) is composed of limestone (ca. 5.5 m thick) and anhydrite (ca. 2.5 m thick) which is overlain by more than 1,115 m of halite, followed by 100 m of sylvine and ca. 1 m of anhydrite. The Z1 reflector corresponds to the transition of the Staßfurt salt to the underlying anhydrite (Fig. 5). The 3rd Zechstein cycle is represented by the Leine Formation. At the base, a couple of meters of dolomitic mudstones are present, followed by 45 m of anhydrite and 150 m of halite with an intercalation of 6 m thick clayey anhydrite. The impedance contrasts of the anhydrite of the Leine Formation and the rock salt of the Staßfurt formation cause another strong reflector (X3 or the so called “Z3 stringer” for the third Zechstein evaporation cycle (Table 2). The Aller and Ohre Formations represent the youngest two cycles of the Zechstein succession in Groß Schönebeck. Above a few meters of clayey and anhydritic sediments, salt rocks are present: ca. 50 m and 12 m in the Aller Formation and the Ohre Formation, respectively. The mapped X1 reflector corresponds to the anhydrite / rock salt succession near the top of the Zechstein. Figure 8C shows the thickness distribution of the Zechstein deposits that clearly outlines the anticlinal structure underneath Groß Schönebeck.

At the top of the anticlinal structure, a pronounced graben-like structure is present in the X3 horizon. The main faults are located ca. 1 km north of the E GrSk 3/90 borehole and is NW-SE oriented (Fig. 9A, B), showing an offset of up to ca. 30 meters. This feature is one to more than two kilometres in length and exhibits a complex and circular fracture pattern at its SE margin. Because this pattern could not be mapped seismically in the overburden it is interpreted as an internal anhydritic and compact Zechstein stringer, overflowed by rock salt that is more mobile. At the base of Zechstein (Z3), no basal faults are visible in the seismic volume (Fig. 9C, D).

Post-Permian

A number of continuously existing reflectors exists in the post-Permian succession. Most prominent are the S1 and S2 reflectors, the M1 and M2 reflectors, and the L2 and B2 reflectors (Fig. 5). In the seismic volume, those reflectors are very well developed in the southern area of the survey. They are less distinct north of the GrSk drillsite. Here, different effects are assumed to be responsible for this loss in quality of the seismic signal: the fracture zone indicated by the broken X3 stringer at the top of the anticlinal structure may extend towards the overburden and account for a scattering and damping of the seismic signal. The graben-like structure, clearly visible in the uppermost Zechstein, is not very distinct in the post-Permian succession. The less developed continuity of the seismic reflection horizons in the northern part of the study area, clearly visible in the CRS PreSDM volume, may reflect a fault system related to the deeper Zechstein salt pillow evolution, but not resolved in the 3D seismic data.

Based on the seismic interpretation, the thickness distribution of the Mesozoic and Cenozoic sediments allows an interpretation of the salt pillow evolution. The Buntsandstein thickness shows a mean of 825 m within a variability of 780–880 m. Its distribution seems to be unrelated to the later salt structure (Fig. 10A). Only in the south eastern and south-western corner of the study area, slightly enhanced thicknesses may indicate a first initiation of the salt

structure development. The thickness of the Muschelkalk (Fig. 10B) shows a more generalized distribution pattern with larger thicknesses in the south and decreasing thicknesses towards the top of the anticlinal structure. The Muschelkalk thickness shows thereby a maximum variation (difference) of up to 120 m in the study area. An intense evolution of the salt structure is documented by the Upper Triassic (Keuper) sedimentary thickness distribution (Fig. 10C). The development of salt rim depression zones, where salt migrates towards the anticlinal structure, allows the sedimentation of greater sediment thicknesses while the sedimentary thickness is reduced on top of the salt structure. This trend continues for the Jurassic and Cretaceous sediment thicknesses (Fig. 10D and 10E), indicated by the slightly increasing variation of the sedimentary thickness for the both units. The Tertiary sediment thickness is affected by the salt pillow topography and by the Quaternary occurred glacial overprint, resulting in the erosion of Tertiary sediments (incision trough, Fig. 10F).

Reservoir model

The established structural model enables the framework for a new Rotliegend reservoir model for further site development. The model comprises the Permo-Carboniferous volcanic rock section and the sedimentary Rotliegend. The geological modelling of the involved structural units and facies types represents the first step of the model construction. In a second step, we parameterized the respective units according to the available borehole and laboratory data.

Determination of parameters for facies modelling

Permo-Carboniferous volcanic rocks

The sequence encountered in the E GrSk 3/90 borehole consists of several layered lava beds and tuffs showing a single bed thickness of one to over three meter (based on core and microresistivity borehole image analysis, Fig. 11). Whereas the top of the volcanic sequence is well preserved by cores showing the transition to the conglomeratic deposits of the Havel Formation, the base of the volcanic sequence and hence its thickness is not proven by the available data. The volcanic rocks encountered in the E GrSk 3/90 borehole are of andesitic composition and show only subordinate fracturing. The rocks cored exhibit an amygdaloidal structure with variable crystal sizes. According to the observed effusive bed thicknesses, the unit was parameterized layer-wise with a vertical resolution of about 2–3 m. Where volcanic bed boundaries could be observed in the borehole image log, they were picked, indicating an N to NNW oriented mean flow direction of the andesitic lava (330°). The thickness of a single volcanic layer amounts to about 30 cm for a tuff layer to about 7 m for an andesitic lava bed. Lavas do clearly dominate over pyroclastic deposits and the mean dip of the surfaces amounts to 15° (showing a range of 5 to 60°). Therefore, it is expected that the Groß Schönebeck site is located in a near-medial to a near central proximal distance to the volcanic vents according to Bogie & Mackenzie (1998) and that the general volcanic succession will not change fundamentally within the modelled seismic volume. However, the overall thickness of the sequence is questionable, and therefore the composition and structuring of the sequence beyond well control is provisional. Following the hitherto assumptions (see section "Permian" above and, e.g., Holl et al., 2005), the sequence may show a thickness of about 70 m or more than 200 m. We set up two models, one considering a thickness of 70 m (model A, shown in the following) and one considering a thickness of 200 m (model B, see discussion) based on the weak seismic reflector observed at a depth level of about 4.4 km.

Sedimentary Rotliegend

For reservoir simulation, four different sedimentary facies types were considered (Fig. 11, Table 3). Most of the coarse-grained bed-load dominated and conglomeratic deposits of the Havel Formation are interpreted as multi-storeyed channel sediments of a *braided plain fluvial* system with a paleocurrent direction towards NNE (Holl et al., 2005). To investigate the geometrical setting of this fluvial system, mean and deviation of cross-bed thickness were determined from the borehole image log of the E GrSk 3/90 borehole (0.59 m and 0.27 m, respectively). This may reflect a paleochannel depth of about 9 m (see Bridge and Tye (2000); Leclair and Bridge, 2001) and correlate to a channel belt width of about 3500 m according to Bridge and Mackey (1993). As our study relies on data from one borehole (E GrSk 3/90) only and the used equations cover a huge spectrum of very different fluvial systems (see, e.g., Gibling, 2006) and have considerable errors, the deduced geometrical parameter given in Table 3 represent a rough estimation of a principal architecture.

The second facies element represents the *ephemeral stream floodplain* environment identified by Holl et al. (2005) for the Dethlingen Formation. As described by the authors, the fine- to coarse-grained sandstones are amalgamated in character and show fining-upward trends to the top of the formation, representing proximal to distal fluvial facies. Transport direction is towards W and NW (265–305°). Within the lower part of the Dethlingen Formation the ERS is developed and shows small to large-scale cross-bedded and low-angle cross-bedded sandstones as well as horizontally laminated sands (Fig. 11). The sediments are interpreted as fluvial reworked aeolian deposits. The estimation of the geometrical architecture of the stream floodplain based on borehole interpretation shown in Table 3 is based on a mean bed thickness and thickness deviation of 0.32 m and 0.2 m. Bar thicknesses, estimated from log data, showed a range of 4–8 m, giving some support for the interpretation. Based on the higher resolution of the DAS-VSP seismic data, Martuganova et al. (2022) could map a 20–30 m thick horizon within the Dethlingen Formation, which they interpreted as a higher porous sandy reservoir section, possibly representing the seismic visible part of a stacked channel architecture. However, internal channel structures are not resolved by the data that is itself limited to the near-borehole area. We therefore use this information as a depth-related trend volume to guide the petrophysical modelling of the ERS, demanding for higher porosities in this zone (see also next section).

The sandy mudflat and mudflat facies types of the Dethlingen and Hannover Formation were represented by finer siliciclastics, indicating the transition to the Zechstein transgression. Borehole image logs are not available for this section. For the *sandy mudflat* environment, siltstone and fine-grained sandstones are present which are interpreted as deposits of sporadic higher current velocities in channel-like structures, assuming the architectural parameters presented in Table 3 (inspired the range for crevasse channels given by Gibling, 2006). The *mudflat facies* finally consists of mudstones of the playa environment without channels.

Parameter compilation for petrophysical modelling

Permo-Carboniferous volcanic rocks

The petrophysical properties of this sequence was evaluated based on the available laboratory measurements of porosity, permeability, thermal properties including density, and log analysis (Fig. 11). Because only GR and Sonic logs and limited core material are available for the lowermost section of the borehole, the core-log analysis of this section represents a first order estimate. For the evaluation of permeability, we used a correlation given by Siratovitch et al. (2014) for andesitic rocks of the Taupo Volcanic Zone in New Zealand. They establish a relation between connected porosity and permeability for the Rotokawa andesite which we applied to our data (dotted line in Fig. 11), showing a quite reasonable match with the laboratory determined permeabilities. Based on the estimated permeability, its anisotropy was calculated as the ratio between the harmonic and the arithmetic averages for 2-m depth intervals (see Table 4a). The thermal conductivity for the igneous rock section was determined using the well-log approach of García et al. (1989) developed for andesitic rocks for the Los Azufres geothermal field in Mexico. They used thermal conductivity measurements under ambient conditions on dry core samples, showing similar values as on andesitic samples of the Northeast German Basin, and correlate them with sonic and density well-log data. To apply their approach on the log data of E GrSk 3/90, we calculated porosity and density from the sonic log based on correlations derived from measurements of Siratovitch et al. (2014). Specific heat capacities of the volcanic rock section were calculated using a formula provided by Heap et al. (2020), developed for andesitic rocks of Mt. Ruapehu in New Zealand based on porosity, bulk and matrix density. Because the approach provides ambient thermal conductivity values, not considering in-situ pT conditions, corresponding corrections were considered. Thermal conductivity was corrected using the pT corrections of Emirov et al. (2017) and Segikuchi (1984), respectively. Heat capacities were T-corrected using the approach of Waples & Waples (2004) and thermal diffusivity calculated based on the corrected thermal conductivity and heat capacity values and the estimated density log.

In terms of petrophysical properties, the tuffite and the andesitic lava beds most likely exhibit some differences (Fig. 11) which could not be evaluated further based on the available data quality. Total porosity (PHIT) of the igneous section was modelled facies-dependent for the modelled layers based on the input data given in Table 4. As a next step, bulk density (BD), effective porosity (PHIGE), and fluid permeability (PERM) were simulated considering the PHIT distribution (using the collocated co-Kriging function, see Table 4a). The thermal conductivity (TC) of the succession was estimated by the approach of García (1989) using the attributed PHIT and BD distributions and applying the same pT-corrections as in the log interpretation. Finally, the expected in-situ SHC was deduced in the same way as for the log interpretation referring to the simulated PHIT and BD distributions and using the approach of Heap et al. (2020) and corrections mentioned above. Finally, the TD of the igneous rocks was derived from the so far determined properties with $TD = TC/(SHC*BD)$.

Table 3
Input data and ranges for facies simulation.

Unit	Stratigraphy	Modelled	Depth range [m]	Background	N/G ratio	Main	Range and mean (channels)				
							facies	[dec]	lithology	Orientation [°]	Amplitude [km]
7	Upper Hannover Fm. (Mellin)	(sandy mudflat)	3875–3901	mudflat playa	0.02	mudstone	like sandy mudflat in unit 5				
6	Hannover Fm. (Mellin-Peckensen)	sandy mudflat	3901–3941	mudflat playa	0.1	mudstone, siltstone, and some sandstone	like sandy mudflat in unit 5				
5	Dethlingen to Hannover Fm. (Peckensen-Eldena)	sandy mudflat	3941–4084	mudflat	0.4	siltstone, fine-grained sandstone	275–360 (300)	0.8–2.5 (1.5)	1.0–5.0 (2.5)	0.005–0.4 (0.06)	0.2–8.0 (2.0)
4	Dethlingen Fm. (Eldena)	ephemeral stream floodplain	4084–4134	sandy mudflat	0.85	siltstone, fine-grained sandstone	200–360 (290)	0.6–2.5 (1.7)	2.0–8.0 (4.0)	0.7–3.3 (2.1)	4.0–8.0 (6.0)
3	Dethlingen Fm. (Rambow, ERS)	ephemeral stream floodplain	4134–4185	sandy mudflat	0.99	fine- to coarse grained siltstone	225–340 (290)				
2	Mirow Fm. (Havel subgroup)	braided river	4185–4222	sandy mudflat	0.8	coarse-grained sandstone and conglomerate	290 (-70) – 90 (345)	0.6–2.5 (1.7)	2.0–8.0 (4.0)	2.5–4.5 (3.5)	8.0–12.0 (9.0)
1	Permo-Carboniferous	tuffite, massive andesite	4222–4292	none	0.85	amygdaloidal andesitic rocks	290 (-70) – 45 (355)	-	-	several km	0.3–7.0 (2)

Table 4: Input parameter used for petrophysical modelling.

a) Volcanic rock section

Facies	bed thickness	range and mean							Variogram input (major/minor/vertical [m], azimuth [°])
		PHIT [dec]	PHIGE+ [dec]	BD** [kg/m ³]	PERM [mD]	TC [Wm ⁻¹ K ⁻¹]	TD [10 ⁻⁶ m ² s ⁻¹]	SHC [Jkg ⁻¹ K ⁻¹]	
Lithology	[m]								
Tuffitic layers	0.3–2.9 (1.4)	0–0.13 (0.04)	0–0.06 (0.02)	2420–2890 (2660)	0–0.09 (0.01)	1.9–2.1 (2.0)	0.73–0.79 (0.77)	960–985 (979)	2000/1500/2, 330
Andesitic lava beds	0.4–7.0 (2.2)	0–0.11 (0.04)	0–0.08 (0.02)	2460–2820 (2630)	0–0.06 (0.01)	1.8–2.1 (2.0)	0.75–0.80 (0.79)	971–985 (983)	2000/1500/3, 330

b) Sedimentary Rotliegend

Facies	Range and mean							Perm [mD]	R ² of PERM	Perm anisotropy	Variogram input (major/minor/vertical [m], azimuth [°])
	PHIT [dec]	PHIGE+ [dec]	BD++ [kg/m ³]	Vshale+++ [dec]	TC [Wm ⁻¹ K ⁻¹]	TD [10 ⁻⁶ m ² s ⁻¹]	SHC [Jkg ⁻¹ K ⁻¹]				
Braided plain fluvial	0–0.16 (0.05)	0–0.05 (0.0)	2510–2690 (2590)	0.1–0.6 (0.2)	2.4–3.7 (3.2)	1.17–1.70 (1.49)	640–920 (805)	6662000 · PHIT ^{8.237}	0.86	0.6	500/250/5, 345
Ephemeral stream floodplain	0–0.21 (0.11)	0–0.18 (0.08)	2280–2690 (2450)	0.01–0.5 (0.1)	2.4–4.0 (3.4)	1.19–1.81 (1.50)	650–1335 (1035)	22050000 · PHIT ^{8.421}	0.93	0.4	500/150/10, 290
Sandy mudflat	0–0.17 (0.05)	0–0.11 (0.03)	2510–2740 (2660)	0.01–0.7 (0.3)	1.6–4.0 (2.9)	0.83–1.85 (1.39)	490–1010 (840)	3965 · PHIT ^{5.794}	0.61	0.2	1500/1000/5, 290
Mudflat playa	0–0.18 (0.04)	0–0.01 (0.0)	2630–2750 (2710)	0.01–0.8 (0.5)	1.5–3.7 (2.3)	0.74–1.76 (1.11)	580–1335 (865)	24020 · PHIT ^{6.613}	0.86	0.2	1500/1250/15, 300

+ Collocated co-Kriging with total porosity (PHIT) using a correlation coefficient of 0.8, ++ Collocated co-Kriging with total porosity (PHIT) using a correlation coefficient of -0.8, +++ Collocated co-Kriging with effective porosity (PHIGE) using a correlation coefficient of -0.8, # estimated for a vertical grid size of 1 m.

Sedimentary Rotliegend

For the evaluation of petrophysical properties, we could rely on the extensive data set of the E GrSk 3/90 borehole. Routine core analysis of the industry provided porosity and density measurements for 200 core plugs, while gas permeability measurements were determined for a sub-volume of 107 plugs. The dataset was extended by further measurements on 29 additional core plugs conducted for enhanced characterization of the site after re-opening of the well. Porosity from well logging was determined using density and neutron logging (Fig. 11). Permeability is shown from single borehole logging (via pulsed-neutron logging, PNL) and based on implementation of the Coates equation. Prior to application of the Coates equation, laboratory gas permeabilities were corrected for in-situ conditions differentiating between three permeability levels (< 160 mD, 160–660 mD, > 660 mD) using the approach of Juhasz (1986). The resulting core data and the log data was then used to establish a permeability relation after Coates et al. (1991). The constants for the Coates relation are found to amount to 750, 6, and 1.4, for a, b, and c, respectively. The derived Coates permeability log shows a general agreement with the permeability estimated by the PNL, but in general a better agreement with the in-situ corrected laboratory-derived permeability data. The comparison of core and log data (Fig. 12) shows in general a very similar distribution, the paired quantile-quantile plot of the effective permeability shows, however, that the log-derived permeability of permeabilities less than 1 mD deviates from the corrected core data, providing slightly higher permeabilities. Anisotropy of permeability was calculated as the ratio between the harmonic and the arithmetic averages of log-derived permeability. Anisotropy ranges from 0.2 to 0.6 for a grid size of 1 m, depending on the respective facies (Table 4b). Log-derived thermal conductivity was calculated using the neutron-neutron, the sonic, and the gamma ray (Vshale) log, thermal diffusivity was estimated based on the neutron-neutron and the gamma ray (Vshale) log, and specific heat capacity was evaluated using the neutron-neutron, the gamma density, and the gamma ray (Vshale) log according to Fuchs et al. (2015). In Fig. 11, the thermal properties based on log estimates are compared to in-situ corrected laboratory measurements. The laboratory derived data was corrected to the respective pressure and temperature conditions by applying the formula of Emirov (2017) and Somerton (1992) for ambient thermal conductivity, the temperature-correction given by Waples and Waples (2004) for specific heat capacity (assuming that pressure is of minor influence on the heat capacity), and calculating the thermal diffusivity based on the in-situ thermal conductivity, temperature corrected heat capacity, and respective laboratory-derived density.

Reservoir modelling

In order to model the distribution of petrophysical properties within the sedimentary succession, we firstly addressed the total porosity (PHIT). Depending on the respective facies, the PHIT distribution was modelled using the geostatistical input provided in Table 3. For the ERS, the seismic facies analysis of Bauer et al. (2020) and the DAS-VSP analysis of Martuganova et al. (2022; for the near-borehole area only) were used as additional trend information for the general probability of higher porosities in the sandy reservoir section. PHIGE of this unit was modelled in relation to PHIT using the collocated co-kriging algorithm of Petrel (Table 4). For a representative and consistent parameterization with permeability and thermal properties, bulk density (BD) of the rocks and the clay content (Vshale) were assigned to the grid cells. They were simulated based on the distribution of PHIT (for BD) and of PHIGE (for Vshale) using the input

parameters specified in Table 4b. PERM was calculated on PHIT (Table 3) and TC was estimated using the BD and Vshale distributions, while the TD distribution was predicted based on Vshale (formulas after Fuchs et al., 2015) and on an empirical correlation with the TD obtained at the borehole log interpretation (based on Vshale and NN, see above). The SHC of this section was calculated using the estimated distributions of TC, TD, and BD according to $SHC = TC/(TD*BD)$.

Figure 13 illustrates the facies-dependent parameterization of the geological model, addressing the mentioned petrophysical properties. In the vertical distribution of the modelled properties, the Permo-Carboniferous volcanic rock sequence (unit 1) at the model bottom shows clearly a layered character, low porosities and different thermal properties than the overlying sedimentary units. The dense conglomeratic rocks of the Mirow Formation (unit 2) show similar bulk densities as the volcanic rocks, but show considerably different transient thermal properties compared to the adjacent model units (13 h, i). Unit 3 (Dethlingen Formation), containing the ERS, is most prominent by showing the best hydraulic properties. The formations above unit 3 are characterized by fine-grained sediments of playa and mud-flat environments, resulting in higher shale content, lower specific heat capacities, and with overall much poorer reservoir properties (Fig. 13). Although the thickness of unit 3 is more or less constant along the section shown in Fig. 13, the parameter of the facies model provokes also some lateral and vertical variation in the property distribution. The lateral variation is also guided by the seismic facies analysis for the ERS, indicating areas of higher porosity or thickness of the ERS. Figure 14 shows the modelled thickness and the distribution of PHIT, Vshale, PERM, and TC, guided by the seismic facies analysis and the interpreted geophysical and laboratory data.

Discussion

The new 3D seismic of the Groß Schönebeck area (Fig. 15) allows a more detailed interpretation of the geological structures of the subsurface and provides a solid framework for the site model building and its petrophysical parameterization.

Structural information

The structural interpretation shows some very distinct and clear features, like the salt pillow distribution pictured by the pronounced Zechstein reflectors, and more ambiguous elements like the base and thickness of the Permo-Carboniferous volcanic sequence.

The top of the volcanic sequence is often well recognizable in seismic sections (Rieke et al., 2001) due to their contrast in the acoustic behaviour of the overlying clastic Rotliegend sediments. However, the base could most often not be deciphered in seismic data. Also for the Groß Schönebeck area, the base of the volcanic rocks could not clearly correlated to a seismic event. The assumed top of Carboniferous as interpreted for the E GrSk 3/90 well were triggered by geophysical log interpretation for the lowermost logged section, postulating that the deepening of the E GrSk 3/90 well already drilled sedimentary rocks of Carboniferous age (Holl et al., 2005). In a first glance, the results of Regenspurg et al. (2016) seems to support this interpretation. They refer to geochemical analysis of drill cuttings from the Gt GrSk 04/05 well which would classify the volcanic rock as dacite or rhyodacite according to the TAS Diagram (Le Maitre et al., 2002). These rock types could relate to the first (oldest) eruption stage in Brandenburg and would therefore support the interpretation that the sedimentary Carboniferous may be present closely. However, further analysis performed on core samples of the correspondent depth interval from the adjacent E GrSk 3/90 borehole classify the cored volcanic rock as andesite (Lotz, 2004). Thus, they may represent the latest eruption stage instead. An explanation for this contradiction could result from a potential contamination of the drill cuttings of the Gt GrSk 4/05 well. Due to a large open-hole section, the finely grounded cuttings (not allowing to depict any rock fragments or structures) may be enriched with silica minerals (quartz) from the sedimentary overburden. There are further indications that the overall thickness of the volcanic sequence accounts for more than 70 m. Bauer et al. (2010) analysed seismic wide-angle data around the Groß Schönebeck site and modelled a reflector in a depth of about 4.7 km which is interpreted to correlate to the top of the Pre-Permian. Taking the uncertainty in depth conversion and the different seismic data types into account, this depth does better match the lower C1 reflector (scenario B) with a depth of about 4.4 km than to the upper C1 reflector (scenario A) with a depth of about 4.2 km. This upper C1 horizon may represent an internal feature of the volcanic succession (intermediate sedimentary layer or tuffite) rather than the top of the (sedimentary) Carboniferous. Greater volcanic thicknesses were also expected by former studies. Benek et al. (1996) and Benek & Hoth (2004) assumed a thickness of 200–400 m for the study area, a range that is also in agreement with legacy exploration data of the former GDR estimating a thickness of about 250 m (Hoth, K. & Huebscher, H.-D., 1986, unpublished map of the expected thickness and lithological succession of the volcanic sequence "Vulkanite Norden DDR"). The different thickness scenarios will have an impact on the further site development. Therefore, a proper seismic-well tie for the top of Carboniferous would be of high relevance. One way to access this data could be achieved by deepening of the E GrSk 3/90 well by coring. Even if Carboniferous rocks were encountered, their characterization would allow an optimized development of an EGS.

For the sedimentary Rotliegend, the 3D seismic provides evidence that faults with large offsets are apparently absent in the study area. Based on the analysis, the Rotliegend of the studied area does not show any segmentation into fault blocks. This is in contrast to the previous assumptions of a pronounced Rotliegend fault system in that area (e.g., Moeck et al., 2009). The supposed faults, interpreted on re-processed 2D seismic lines using complex attribute analysis, could not be confirmed by the 3D seismic volume. The existing of large and pronounced fault systems, at least in the order of the resolution of the 3D seismic, were not present in the data. Subseismic joints and faults are, however, expected. Interpretation of microseismic events due to hydraulic stimulations (Kwiatek et al., 2010) do suffer from the challenges in accurate location of the events but give some ideas on the possible orientation of fault planes. The events, however, do not coincide with structures within the seismic volume (Fig. 16A). In this context it is of interest that Blöcher et al. (2018) assume the existence of a fault along the microseismic events, but they also state that they would expect seismic events for two former interpreted faults nearby the stimulated area, which did not occur. In consequence, they questioned their existence. This interpretation, which is based on a numerical model of coupled thermal-hydraulic-mechanical processes for accessing the fault reactivation potential and its alteration during a waterfrac stimulation treatment, is in agreement with the results from the 3D survey (Krawczyk et al., 2019) where no distinct faults could be mapped.

Our study allows some further information on the timing and evolution of the salt pillow of Groß Schönbeck, which started in the Upper Buntsandstein and continues in the Cretaceous to Cenozoic. The mapped graben structure at the top of the anticline (related to the X3 horizon) are interpreted as internal Zechstein structures, resulting from broken anhydritic layers which were passed by more ductile rock salt. A similar process is described by Strozyk et al. (2012) for the western Dutch offshore for the so-called Z3 stringer (corresponding to the anhydrite of the Leine formation, reflector X2 to X3). This interpretation is also supported by the fact, that the post-Permian reflectors do not show any distinct fault patterns in the 3D seismic. The uppermost reflector that could be tracked more or less completely in the volume is the Jurassic L2 reflector. The seismic to well-tie (Fig. 5) relies on several types of input data and is expected to represent a robust interpretation, especially for depths below 0.5-1 km. Comparing different time-to-depth conversions and former interpretations on legacy seismic data, this uppermost depth level shows often slightly different correlations for the seismic horizons. However, signal strength and resolution do not allow a detailed interpretation of the structural and internal layering of post Jurassic strata. Former interpretations based on one 2D seismic section reaching into the northwest of the 3D seismic area (e.g., LEW25/01, Figs. 1, 16B/C) show some discontinuous reflectors (courtesy Neptune Energy). The 3D seismic could not resolve visible faults, however, the overall seismic signal is reduced in that area. This may indicate a somehow distorted layering of the strata or just be related to a worse acoustic coupling due to higher thicknesses of younger sediments with low densities. From surface studies, Hardt et al. (2021) interpret Quaternary landforms to result from the interaction of glacial tectonics and halo tectonics. Their location corresponds to the area where the deep fracture are assigned in the 3D seismic volume. Besides acoustic scattering triggered by a fracture system, significant changes in the near-surface geology may represent another factor affecting the quality of the seismic signal within the post-Permian. Figure 17 shows the thickness distribution of Quaternary sediments in the study area and the thickness of the Tertiary Rupelton according to Stackebrand & Manhenke (2010). In the northwestern part of the study area, a Quaternary incision trough cuts into the Tertiary Rupelton allowing the deposition of more than 200 m-thick unconsolidated Quaternary sediments, while the mean Quaternary sediment thickness in the remaining area amounts to about 50–75 m (Fig. 17A). In the area of the incision trough, the seismic signal is less pronounced like for the northern part of the seismic volume. However, no deep fractures are observed in the Zechstein reflectors here. The Quaternary incision trough also reduces the thickness of the Tertiary Rupelton that shows a more complex distribution (Fig. 17B). The increased thickness of the Rupelton north of the Groß Schönebeck drillsite coincides partly with the assumed fractured area and may cause an additional damping of the seismic signal (Fig. 17C). In general, the seismic coverage decreases towards the surface, introducing some artefacts in the seismic volume and artificial discontinuities of the shallower seismic reflectors (Fig. 5).

Facies interpretation and model parameterization

The modelled facies and parameter distribution is aiming to reflect a realistic scenario of lateral and vertical structural and property distribution. The main restriction of the model is that the interpretation of the sedimentary facies of the Rotliegend needs to focus more or less on one location within the seismic volume (E GrSk 3/90 and Gt GrSk 4/05 boreholes) and that the volcanic sequence is not characterized by the wells completely.

The volcanic succession and a realistic property distribution is difficult to define. As the top of the sedimentary Carboniferous could not be resolved for sure, neither from seismic or borehole data, this interpretation is lacking important input data. In addition, it seems more realistic, that several volcanoes are building up this sequence, resulting also in a more diverse flow and property distribution pattern of intercalated flows. Therefore, the presented interpretation and parameterization of the volcanic sequence represents a first-order approximation to enable further near-wellbore studies for site development, helping in identifying possible layouts and related risks of hydraulic stimulations and in estimating the geothermal potential of this sequence. As stress in the subsurface is expected to increase with depth, an upward fracture growth could be expected (see also Fig. 5 in Zimmermann et al., 2010). By stimulating the volcanic rock sequence, the fracture will tend to grow towards the overlying sedimentary Havel Formation consisting of conglomerates and sandstones. Due to the different hydraulic and mechanical properties, the fracture will tend to inflate into these overlying units and further fracture growth in the volcanic sequence will be limited. Therefore, a larger thickness of the volcanic rocks will increase the possible fracture length growth before the fracture crosses towards the higher permeability, weaker and less stiff overlying sedimentary rock units, which will reduce the treatment efficiency due to out-of-zone fracture growth and excessive leak-off. In order to be in a position to design an adequate stimulation treatment of the volcanic rock series, its real thickness and composition (heterogeneity) needs to be investigated in more detail. One option represents the deepening of the E GrSk 3/90 borehole by coring and logging until proven Carboniferous rocks were encountered.

The sedimentary Rotliegend could rely on a much broader data set. Several boreholes nearby give evidence on the principal composition and the development of the sedimentary environment over time. The petrophysical well-log and core analysis reveals a profound facies-dependency of petrophysical properties. Focusing on the permeability characterization, the most robust correlation of porosity and permeability could be found in the ephemeral stream facies. This is in agreement with the mineralogical composition of the corresponding sandy reservoir: it represents a Quartz-dominated sandstone, and the permeability is not strongly affected by clay minerals. The proportion of clay minerals and their textural properties plays a larger role for other sandy facies units, like the braided plains or sandy mudflat environment. The derived in-situ fluid permeabilities for unit 5 (ERS) ranges from less than 1 mD to more than 100 mD, with an overall geometric mean of only some mD (Figs. 13, 14). The analysis of well tests at the Groß Schönebeck site (Blöcher et al., 2016) reports in the appendix transmissibility data of several hydraulic tests conducted. If we assume a reservoir thickness of the EBS of roughly 40 m at the wellsite, corresponding field permeabilities were in the same order, showing values of about 4 mD.

Although the seismic data could not provide evidence for structural boundaries (block or fault compartments), the result of the facies and parameter modelling shows for unit 5 (EBS) slightly reduced reservoir properties along the Gt GrSk 4/05 borehole (Fig. 14). The range of variation is covered by the expected geological heterogeneity. However, the reconstruction of ancient fluvial system requires detailed information on its geometry in three dimensions. Former realizations did not consider the natural heterogeneity of the Permian reservoir but apply a layer-cake model of petrophysical properties, without consideration of lateral variability (Blöcher et al., 2016). The presented new model will be used for reservoir simulation, comparison, and future site development. First studies using a more realistic heterogeneous parameterization inspired by this study show that this may lead to a significant change in the long-term behaviour of the reservoir compared to a layer-cake model, allowing a much faster breakthrough along preferred flow paths, requiring a different

well doublet layout. Moreover, the productivity of the system could be increased by an adapted exploitation concept, considering the real property distribution (Bohnen, 2020).

Further enhancement of the presented model parameterization could be arrived by inversion of the seismic data to better guide the distribution of petrophysical parameters. The inversion of the seismic volume may give some further insights on the property distribution patterns and reservoir heterogeneity. Nevertheless, the inversion will also be limited by the scale and resolution of the geophysical (seismic) data and will not be able to resolve a detailed geological facies pattern and the accompanied petrophysical properties on a finer scale.

Conclusions

This work presents the results of an integrated study for reservoir characterization of a long-lasting deep geothermal research platform Groß Schönebeck by integrating new geophysical data. Reservoir characterization by geological modeling is scale-sensitive. Integrating the available reconnaissance data with interpretations from the new 3D seismic survey and the DAS-VSP data and the borehole data allows constraining a much more realistic characterisation of the Rotliegend reservoir of the Groß Schönebeck research platform across different scales. Based on the structural data from 3D seismic and DAS-VSP geophysics as well as considering the geological (lithological and sedimentological) data from the boreholes, a new site and reservoir model was set up, following a facies-dependent distribution approach for its parameterization. In more detail, the new data allows a remapping of the thickness of the sandy EBS reservoir zone and adjacent horizons and their reservoir properties. The new 3D seismic data did not show any compartmentalization of the Rotliegend reservoir at the Groß Schönebeck site. Also the cores of the E GrSk 3/90 borehole do not show extensive fracturing. Nevertheless, joints and small faults of subtle and predominantly sub-seismic character may be present in the Rotliegend reservoir target. The thickness of the Permo-Carboniferous volcanic sequence, so far only indirectly derived from geophysical borehole logging in the same well, could not be clearly confirmed by the seismic data. To shed more light into the section below the sedimentary Rotliegend, a deepening of the E GrSk 3/90 borehole, preferably by coring, would allow to judge on the thickness and properties of the Permo-Carboniferous sequence. Further site development could rely on deviated wells in the Rotliegend and Permo-Carboniferous reservoirs with multi-stage stimulation to enhance the productivity of the reservoirs. The provided in-depth characterization is forming the basis for an ongoing evaluation of such and other exploitation strategies for the exploitation of deep geothermal reservoirs in the Northeast German Basin.

Declarations

Availability of data and materials

The datasets used and/or analysed during the current study are available from the corresponding author on reasonable request.

Competing interests

The authors declare that they have no competing interests.

Funding

The seismic survey was funded by the German Federal Ministry for Economics within the project RissDom-A (grant 0324065).

Authors' contributions

BN, KB, and CK analysed and interpreted the geological and seismic data, BN performed the geological modelling and the facies and parameter parametrization of the reservoir targets, and was the major contributor writing the manuscript. All authors read and approved the final manuscript.

Acknowledgements

We thank Neptune Energy for support and the permission to use legacy exploration borehole and seismic data (profiles LEW).

References

1. Ahlrichs N, Hübscher C, Noack V, Schnabel M, Damm V, Krawczyk CM. Structural Evolution at the Northeast North German Basin Margin: From Initial Triassic Salt Movement to Late Cretaceous-Cenozoic Remobilization. *Tectonics*. 2020; doi: 10.1029/2019TC005927.
2. Allen PA, Allen JR. *Basin Analysis – Principles and Applications*. Oxford: Blackwell Science; 1990.
3. Bauer K, Norden B, Ivanova A, Stiller M, Krawczyk CM. Wavelet transform-based seismic facies classification and modelling: application to a geothermal target horizon in the NE German Basin. *Geophys Prospect*. 2020. doi:10.1111/1365-2478.12853.
4. Bauer K, Moeck I, Norden B, Schulze A, Weber M, Wirth H. Tomographic P-wave velocity and vertical velocity gradient structure across the geothermal site Groß Schönebeck (NE German Basin): Relationship to lithology, salt tectonics, and thermal regime. *J Geophys Res*. 2010. doi:10.1029/2009JB006895.
5. Bełka Z, Devleeschouwer X, Narkiewicz M, Piecha M, Reijers TJA, Ribbert KH, Smith NJP. Devonian. In: Doornenbal JC, Stevenson AG, editors. *Petroleum Geological Atlas of the Southern Permian Basin Area*. Houten: EAGE Publications; 2010. pp. 71–9.
6. Benek R, Kramer W, McCann T, Scheck M, Negendank J, Korich D, Huebscher HD, Bayer U. Permo-carboniferous magmatism of the Northeast German Basin. *Tectonophysics*. 1996;266:379–404.
7. Benek R, Hoth P. Permokarbonische Vulkanite. In: Stackebrandt W, Manhenke V, editors. *Atlas zur Geologie von Brandenburg*. Kleinmachnow: Landesamt für Geowissenschaften und Rohstoffe Brandenburg (LGRB); 2004. p. 80.

8. Beutler G, Franz M, Keuper. In: Stackebrandt W, Franke D, editors. *Geologie von Brandenburg*. Stuttgart: Schweitzerbart; 2015. pp. 194–216.
9. Blöcher G, Reinsch T, Henniges J, Milsch H, Regenspurg S, Kummerow J, Francke H, Kranz S, Saadat A, Zimmermann G, Huenges E. Hydraulic history and current state of the deep geothermal reservoir Groß Schönebeck. *Geothermics*. 2016. doi:10.1016/j.geothermics.2015.07.008.
10. Blöcher G, Cacace M, Jacquy AB, Zang A, Heidbach O, Hofmann H, Kluge C, Zimmermann G. Evaluating Micro-Seismic Events Triggered by Reservoir Operations at the Geothermal Site of Groß Schönebeck (Germany). *Rock Mech Rock Eng*. 2018. doi:10.1007/s00603-018-1521-2.
11. Bogie I, Mackenzie KM. The application of a volcanic facies model to an andesitic stratovolcano hosted geothermal system at Wayang Windu, Java, Indonesia. 20th New Zealand Geothermal Workshop. 1998. https://pangea.stanford.edu/ERE/db/IGAstandard/record_detail.php?id=1827. Accessed 16.02.2022.
12. Bohnen B. Investigation of the influence of heterogenous reservoir properties on the productivity and sustainability of the geothermal doublet system Groß Schönebeck. TU Berlin: master thesis; 2020.
13. Breitzkreuz C, Geißler M. Permokarbonische Vulkanite. In: Stackebrandt W, Franke D, editors. *Geologie von Brandenburg*. Stuttgart: Schweitzerbart; 2015. pp. 110–6.
14. Bridge JS, Mackey SD. A theoretical study of fluvial sandstone body dimensions. *Int Assoc Sedimentol Spec Publ*. 1993;15:213–36.
15. Bridge JS, Tye RS. Interpreting the Dimensions of Ancient Fluvial Channel Bars, Channels, and Channel Belts from Wireline-Logs and Cores. *Am Assoc Pet Geol Bull*. 2000;84(8):1205–28.
16. Bunes H, von Hartmann H, Rumpel H-M, Krawczyk CM, Schulz R. Fault imaging in sparsely sampled 3D seismic data using common-reflection-surface processing and attribute analysis – a study in the Upper Rhine Graben. *Geophys Prospect*. 2014. doi.org/10.1111/1365-2478.12099.
17. Coates GR, Peveraro RCA, Hardwick A, Roberts D. The magnetic resonance imaging log characterized by comparison with petrophysical properties and laboratory core data. *SPE Annu Tech Conf Exhib*. 1991. doi.org/10.2118/22723-MS.
18. DEKORP-BASIN Research Group. The deep crustal structure of the Northeast German basin: New DEKORP-BASIN'96 deep-profiling results. *Geology*. 1999. doi.org/10.1130/0091-7613(1999)027<0055:DCSOTN>2.3.CO;2.
19. Doornbal H, Stevenson A. *Petroleum geological atlas of the southern Permian Basin Area*. Houten: EAGE Publications BV; 2010.
20. DSK (Deutsche Stratigraphische Kommission). *Stratigraphische Tabelle von Deutschland 2016*. Potsdam: Deutsches GeoForschungsZentrum. 2016; 1p.
21. Emirov SN, Beybalaev VD, Gadzhiev GG, Ramazanov AE, Amirova AA, Aliverdiev AA. To the description of the temperature and pressure dependences of the thermal conductivity of sandstone and ceramics. *J Phys Conf Ser*. 2017;891.
22. Franke D. Devon. In: Stackebrandt W, Franke D, editors. *Geologie von Brandenburg*. Stuttgart: Schweitzerbart; 2015a. pp. 73–83.
23. Franke D. Flyschoides Karbon. In: Stackebrandt W, Franke D, editors. *Geologie von Brandenburg*. Stuttgart: Schweitzerbart; 2015b. pp. 83–95.
24. Franke D. Molassoides Karbon. In: Stackebrandt W, Franke D, editors. *Geologie von Brandenburg*. Stuttgart: Schweitzerbart; 2015c. pp. 102–9.
25. Fuchs S, Balling N, Förster A. Calculation of thermal conductivity, thermal diffusivity and specific heat capacity of sedimentary rocks using petrophysical well logs. 2015; doi:10.1093/gji/ggv403.
26. García A, Contreras E, Viggiano JC. Establishment of an empirical correlation for estimating the thermal conductivity of igneous rocks. *Int J Thermophys*. 1989. doi:10.1007/BF00503174.
27. Gast RE. 2.6 Sequenzstratigraphie. In: Plein E, editor. *Stratigraphie von Deutschland I - Norddeutsches Rotliegendebcken, Rotliegend-Monographie Teil II*. Frankfurt: Courier Forschungsinstitut Senckenberg; 1995. pp. 47–54.
28. Gast RE, Pasternak M, Piske J, Rasch H-J. Das Rotliegend im nordostdeutschen Raum: Regionale Übersicht, Stratigraphie, Fazies und Diagenese. *Geol Jahrb Reihe A*. 1998;149:59–79.
29. Gast RE, Gebhardt U. 4.4 Elbe-Subgruppe. In: Plein E, editor. *Stratigraphie von Deutschland I - Norddeutsches Rotliegendebcken, Rotliegend-Monographie Teil II*. Frankfurt: Courier Forschungsinstitut Senckenberg; 1995. pp. 121–35.
30. Gast RE, Duser M, Breitzkreuz C, Gaupp R, Schneider JW, Stemmerik L, Geluk MC, Geisler M, Kiersnowski H, Glennie KW, Kabel S, Jones, NS. Rotliegend. In: Doornbal JC, Stevenson AG, editors. *Petroleum Geological Atlas of the Southern Permian Basin Area*. Houten: EAGE Publications; 2010: p.101 – 21.
31. Gebhardt U, Schneider J, Hoffmann N. Modelle zur Stratigraphie und Beckenentwicklung im Rotliegenden der Norddeutschen Senke. *Geol Jahrb Reihe A*. 1991;127:405–27.
32. Geißler M, Breitzkreuz C, Kiersnowski H. Late Paleozoic volcanism in the central part of the Southern Permian Basin (NE Germany, W Poland): facies distribution and volcano-topographic hiati. *Int J Earth Sci*. 2008;97(5):973–89.
33. Gibling MR. Width and Thickness of Fluvial Channel Bodies and Valley Fills in the Geological Record: A Literature Compilation and Classification. *J Sediment Res*. 2006;76(5):731–70.
34. Hardt J, Norden B, Bauer K, Toelle O, Krumbach J. Surface cracks – geomorphological indicators for late Quaternary halotectonic movements in Northern Germany. *Earth Surf Process Landf*. 2021. doi:10.1002/esp.5226.
35. von Hartmann H, Beilecke T, Bunes H, Musmann P, Schulz R. Seismische Exploration für tiefe Geothermie. *Geol Jahrb*. 2015;B104:1–271.
36. Heap MJ, Kushnir ARL, Vasseur J, Wadsworth FB, Harlé P, Baud P, Kennedy BM, Troll VR, Deegan FM. The thermal properties of porous andesite. *J Volcanol Geoth Res*. 2020. doi.:10.1016/j.jvolgeores.2020.106901.
37. Henniges J, Martuganova E, Stiller M, Norden B, Krawczyk CM. Wireline distributed acoustic sensing allows 4.2 km-deep vertical seismic profiling of the Rotliegend 150°C-geothermal reservoir in the North German Basin. *Solid Earth*. 2021. doi:10.5194/se-12-521-2021.
38. Holl H-G, Moeck I, Schandlmeier H. Characterization of the tectono-sedimentary evolution of a geothermal reservoir - implications for exploitation (Southern Permian Basin, NE Germany), (Proceedings), World Geothermal Congress (Antalya Turkey). 2005. <https://www.geothermal->

energy.org/pdf/IGAstandard/WGC/2005/0614.pdf. Accessed 16 Feb 2022.

39. Hoth K, Ruspült J, Zagora K, Beer H, Hartmann O. Die tiefen Bohrungen im Zentralabschnitt der Mitteleuropäischen Senke - Dokumentation für den Zeitabschnitt 1962–1990. Berlin: Schriftenr geol Wiss. 1993;2:145p.
40. Huebscher H-D. Zur epigenetischen Metasomatose in den permosilesischen basaltischen Mg-Andesiten von Ost-Brandenburg, Deutschland. *Terra Nostra*. 1995;7:63–6.
41. Huenges E. Einleitung. In: Huenges E, Hurter S, editors. In-situ Geothermielabor Groß Schönebeck 2000/2001. Scientific Technical Report STR02/14. 2002; doi: 10.23689/fidgeo-522.
42. Huenges E, Hurter S, editors. In-situ Geothermielabor Groß Schönebeck 2000/2001. Scientific Technical Report STR02/14. 2002; doi: 10.23689/fidgeo-522.
43. Juhasz I. Conversion of routine air permeability data into stressed brine-permeability data. SPWLA Tenth European Formation Evaluation Symposium, Aberdeen, UK. 1986;15p.
44. Kana JD, Djongyang N, Raidandi D, Nouck PN, Dadjé A. A review of geophysical methods for geothermal exploration. *Renew Sust Energy Rev*. 2015. doi:10.1016/j.rser.2014.12.026.
45. Kopp J, Hoffmann N, Lindert W, Franke D. Präpermischer Untergrund - Tektonostratigraphie und Bruchstörungen. In: Stackebrandt W, Manhenke V, editors. Atlas zur Geologie von Brandenburg. Kleinmachnow: Landesamt für Geowissenschaften und Rohstoffe Brandenburg (LGRB). 2004: 80.
46. Kombrink H, Besly BM, Collinson JD, Den Hartog Jager DG, Drozdowski G, Duser M, Hoth P, Pagnier HJM, Stemmerik L, Waksmundzka MI, Wrede V. Carboniferous. In: Doornenbal JC, Stevenson AG, editors. Petroleum Geological Atlas of the Southern Permian Basin Area. Houten: EAGE Publications; 2010. pp. 81–99.
47. Kossow D, Krawczyk CM, McCann T, Strecker M, Negendank JFW. Style and evolution of salt pillows and related structures in the northern part of the Northeast German Basin. *Int J Earth Sci*. 2000;89(3):652–64.
48. Kossow D, Krawczyk CM. Structure and quantification of factors controlling the evolution of the inverted NE German Basin. *Mar Pet Geol*. 2002;19(5):601–18.
49. Krawczyk CM, Henk A, Tanner DC, Trappe H, Ziesch J, Beilecke T, Aruffo CM, Weber B, Lippmann A, Görke U-J, Bilke L, Kolditz O. Seismic and sub-seismic deformation prediction in the context of geological carbon trapping and storage. *Adv technol Earth sci*. 2015. doi:10.1007/978-3-319-13930-2_5.
50. Krawczyk CM, Stiller M, Bauer K, Norden B, Hennings J, Ivanova A, Huenges E. 3-D seismic exploration across the deep geothermal research platform Groß Schönebeck north of Berlin/Germany. *Geotherm Energy*. 2019. doi:10.1186/s40517-019-0131-x.
51. Kwiatek G, Bohnhoff M, Dresen G, Schulze A, Schulte T, Zimmermann G, Huenges E. Microseismicity induced during fluid-injection: A case study from the geothermal site at Groß Schönebeck, North German Basin. *Acta Geophys*. 2010. doi:10.2478/s11600-010-0032-7.
52. Lange G, Söllig A, Tessin R, ZGI. Isobathen der Zechsteinbasis 1:500.000. VEB Kartographischer Dienst Potsdam. Berlin: Zentrales Geologisches Institut; 1981.
53. Leclair SF, Bridge JS. Quantitative Interpretation of Sedimentary Structures formed by river dunes. *J Sediment Res*. 2001;71(5):713–16.
54. Le Maitre RW, editor. *Igneous Rocks: A Classification and Glossary of Terms*. Cambridge University Press; 2002. 252p.
55. Lindert W, Warncke D, Stumm M. Probleme der lithostratigraphischen Korrelation des Oberrotliegenden (Saxon) im Norden der DDR. *Z angew Geol*. 1990;36(10):368–75.
56. Lokhorst A. NW European gas atlas. Haarlem: Nederlands Inst. voor Toegepaste Geowetenschappen TNO. 1 CD-ROM; 1998.
57. Lotz B. Neubewertung des rezenten Wärmestroms im Nordostdeutschen Becken. Potsdam: Scientific Technical Report 04/04. 2004. <http://d-nb.info/971558531/34>. Accessed 16 Feb 2022.
58. Martuganova E, Krawczyk CM. 3D deep geothermal reservoir imaging with wireline distributed acoustic sensing in two boreholes. *Solid Earth*. 2022. <https://doi.org/10.5194/se-2021-138>.
59. McCann T. Sandstone composition and provenance of the Rotliegend of the NE German Basin. *Sediment Geol*. 1998; 116(3–4): 177 – 98.
60. McGuire JJ, Lohman RB, Catchings RD, Rymer MJ, Goldman MR. Relationships among seismic velocity, metamorphism, and seismic and aseismic fault slip in the Salton Sea Geothermal Field region. *J Geophys Res Solid Earth*. 2015. doi:10.1002/2014JB011579.
61. Mendrinis D, Chorapanitis I, Polyzou O, Karytsas C. Exploring for geothermal resources in Greece. *Geothermics*. 2010. doi:10.1016/j.geothermics.2009.11.002.
62. Moeck I, Schandelmeier H, Holl HG. The stress regime in a Rotliegend reservoir of the Northeast German Basin. *Int J Earth Sci*. 2009. doi:10.1007/s00531-008-0316-1.
63. Mönnig E. Northern Germany. In: McCann T, editor. *The Geology of Central Europe*. London: The Geological Society; 2008. 842 – 46.
64. Peryt TM, Geluk MC, Mathiesen A, Paul J, Smith K. Zechstein. In: Doornenbal JC, Stevenson AG, editors. *Petroleum Geological Atlas of the Southern Permian Basin Area*. Houten: EAGE Publications; 2010. pp. 123–47.
65. Plein E, editor. *Stratigraphie von Deutschland I - Norddeutsches Rotliegendbecken, Rotliegend-Monographie Teil II*. Frankfurt: Courier Forschungsinstitut Senckenberg; 1995.
66. Pussak M, Bauer K, Stiller M, Bujakowski W. Improved 3D seismic attribute mapping by CRS stacking instead of NMO stacking: Application to a geothermal reservoir in the Polish basin. *J Appl Geophys*. 2014. doi:10.1016/j.jappgeo.2014.01.020.
67. Reinhardt H-G. Structure of Northeast Germany: regional depth and thickness maps of Permian to Tertiary intervals compiled from seismic reflection data. *Spec Publ Eur Assoc Petroleum Geoscientists*. 1993;3:155–65.

68. Regenspurg S, Feldbusch E, Norden B, Tichomirowa M. Fluid-rock interactions in a geothermal Rotliegend/Permo-Carboniferous reservoir (North German Basin). *Appl Geochem*. 2016. doi:10.1016/j.apgeochem.2016.03.010.
69. Ricard LP, Huddleston-Holmes CR, Pujol M. Reservoir and Production Engineering Challenges for Geothermal Systems Hosted in Australian Sedimentary Basins. *Soc Pet Eng*. 2016. doi:10.2118/182343-MS.
70. Rider M. *The Geological Interpretation of Well Logs*. Caithness: Whittles Publ; 2000. 280 p.
71. Rieke H, *Sedimentologie, Faziesarchitektur und Faziesentwicklung des kontinentalen Rotliegenden im Norddeutschen Becken (NEDB)*. Potsdam: Scientific Technical Report STR 01/14. 2001; doi: 10.48440/GFZ.b103-010029.
72. Rieke H, Kossov D, McCann T, Krawczyk CM. Tectono-sedimentary evolution of the northernmost margin of the NE German Basin between uppermost Carboniferous and Late Permian (Rotliegend). *Geol J*. 2001;36(1):19–37.
73. Rieke H, McCann T, Krawczyk CM, Negendank JFW. Evaluation of controlling factors on facies distribution and evolution in an arid continental environment: an example from the Rotliegend of the NE German Basin. In McCann T, Saintot A, editors. *Tracing tectonic deformation using the sedimentary record*. *Geol Soc Spec Publ*. 2003; 208:71–94.
74. Scheck M, Bayer U. Evolution of the Northeast German Basin - inferences from a 3D structural model and subsidence analysis. *Tectonophysics*. 1999;313(1–2):145–69.
75. Scheck M, Bayer U, Lewerenz B. Salt movements in the Northeast German Basin and its relation to major post-Permian tectonic phases—results from 3D structural modelling, backstripping and reflection seismic data. *Tectonophysics*. 2003;361(3–4):277–99.
76. Scheck-Wenderoth M, Maystrenko Y, Hübscher C, Hansen M, Mazur S. Dynamics of salt basins. In: Littke R, Bayer U, Gajewski, D, Nelskamp S, editors. *Dynamics of Complex Sedimentary Basins. The Central European Basin System*. Berlin-Heidelberg: Springer-Verlag. 2008: p.307 – 22.
77. Schudack M, Tessin R. Jura. In: Stackebrandt W, Franke D, editors. *Geologie von Brandenburg*. Stuttgart: Schweizerbart. 2015: p. 217 – 40.
78. Siler DL, Faulds JE, Mayhew B, McNamara DD. Analysis of the favorability for geothermal fluid flow in 3D: Astor Pass geothermal prospect, Great Basin, northwestern Nevada, USA. *Geothermics*. 2016; doi: 10.1016/j.geothermics.2015.11.002.
79. Siratovich PA, Heap MJ, Villeneuve MC, Cole JW, Reuschlé T. Physical property relationships of the Rotokawa Andesite, a significant geothermal reservoir rock in the Taupo Volcanic Zone, New Zealand. *Geotherm Energy*. 2014. doi:10.1186/s40517-014-0010-4.
80. Stackebrandt W, Manhenke V. *Atlas zur Geologie von Brandenburg*. Cottbus: Landesamt für Bergbau, Geologie und Rohstoffe; 2010.
81. Stackebrandt W, Röhling HG. Trias – Geologischer Rahmen. In: Stackebrandt W, Franke D, editors. *Geologie von Brandenburg*. Stuttgart: Schweizerbart; 2015. pp. 144–7.
82. Standke G. Tertiär. In: Stackebrandt W, Franke D, editors. *Geologie von Brandenburg*. Stuttgart: Schweizerbart; 2015. pp. 259–333.
83. Strozyk F, Van Gent H, Urai JL, Kukla PA. 3D seismic study of complex intra-salt deformation: An example from the Upper Permian Zechstein 3 stringer, western Dutch offshore. *Geol Soc Spec Publ*. 2012. doi:10.1144/SP363.23.
84. Strozyk F, Reuning L, Scheck-Wenderoth M, Tanner DC. Chapter 10 - The Tectonic History of the Zechstein Basin in the Netherlands and Germany. In: Soto JI, Flinch JF, Tari G. *Permo-Triassic Salt Provinces of Europe, North Africa and the Atlantic Margins*. Amsterdam: Elsevier; 2017. pp. 221–41.
85. Trautwein U. *Poroelastische Verformung und petrophysikalische Eigenschaften von Rotliegend Sandsteinen*. Berlin: Dissertation TU Berlin. 2005. https://depositonce.tu-berlin.de/bitstream/11303/1537/1/Dokument_47.pdf. Accessed 16 Feb 2022.
86. Trautwein U, Huenges E. Poroelastic behaviour of physical properties in Rotliegend Sandstones under uniaxial strain, *Internat. J. Rock Mech Min Sci*. 2005; 42(7–8): 924 – 32.
87. van Wees J-D, Stephenson RA, Ziegler PA, Bayer U, McCann T, Dadlez R, Gaupp R, Narkiewicz M, Bitzer F, Scheck M. On the origin of the Southern Permian Basin, Central Europe. *Mar Pet Geol*. 2000;17:43–59.
88. Waples DW, Waples JS. A Review and Evaluation of Specific Heat Capacities of Rocks, Minerals, and Subsurface Fluids. Part 1: Minerals and Nonporous Rocks. *Nat Resour Res*. 2004. doi:10.1023/B:NARR.0000032647.41046.e7.
89. Zhang X, Hu Q. Development of Geothermal Resources in China: A Review. *J Earth Sci*. 2018. doi:10.1007/s12583-018-0838-9.
90. Zhang Y, Krause M, Mutti M. The Formation and Structure Evolution of Zechstein (Upper Permian) Salt in Northeast German Basin: A Review. *Open J Geology*. 2013. doi:10.4236/ojg.2013.38047.
91. Ziegler PA. *Geological Atlas of Western and Central Europe, 2nd Edition*. The Hague: Shell; 1990.
92. Zimmermann G, Moeck I, Blöcher G. Cyclic waterfrac stimulation to develop an Enhanced Geothermal System (EGS)—Conceptual design and experimental results. *Geothermics*. 2010. doi:10.1016/j.geothermics.2009.10.003.

Figures

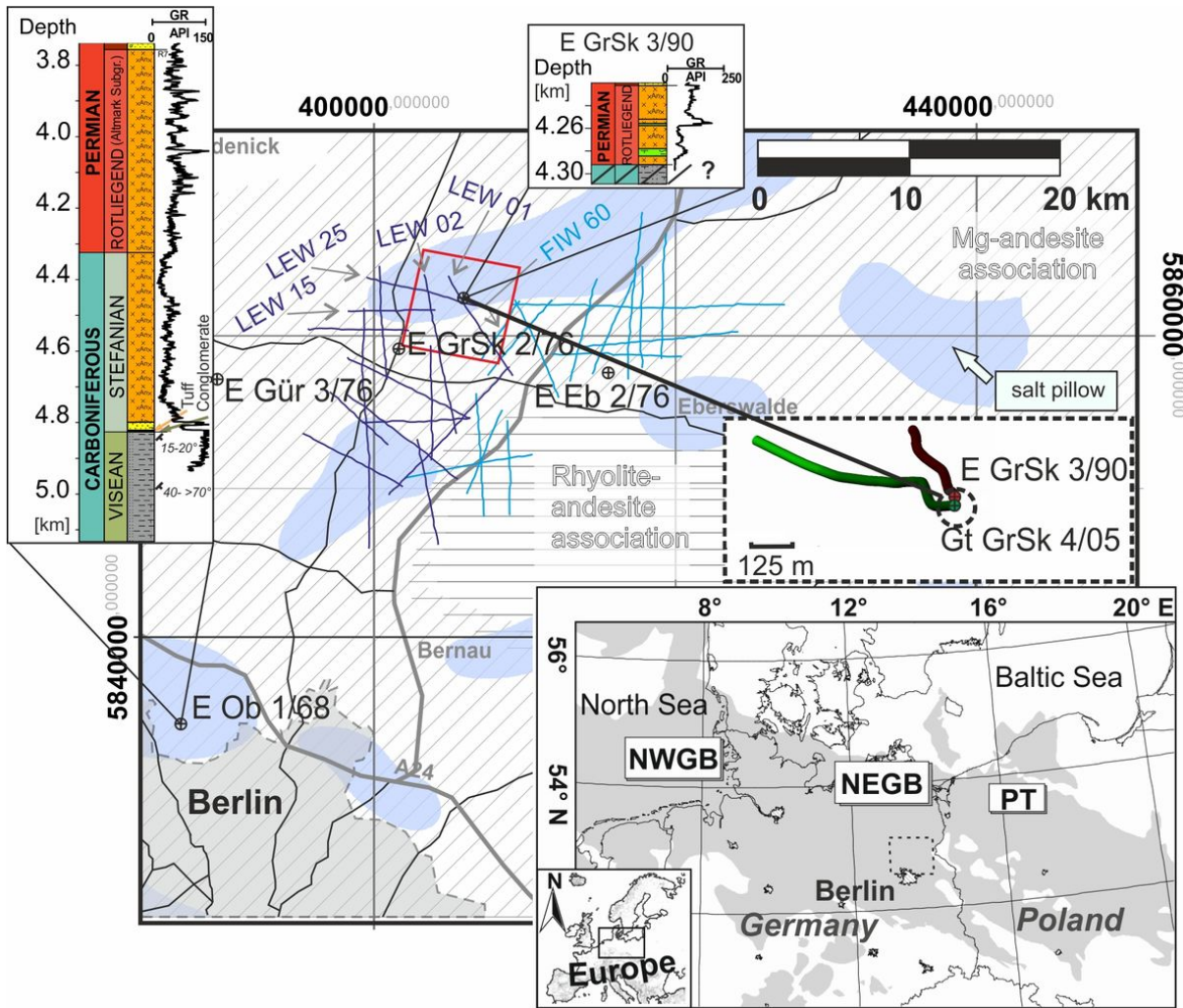


Figure 1
 Site map of Northeast Brandenburg showing the 3D seismic of the Groß Schönebeck study area (red rectangle), the location of former 2D seismic reconnaissance lines, the location of deep boreholes, the distribution of the Permo-Carboniferous volcanic rock associations after Benek et al. (1996), the Permo-Carboniferous succession as encountered in two boreholes (E Ob 1/68 and E GrSk 3/90, for legend see Fig. 2), the distribution of salt pillows in the subsurface according to the Northwest-European Gas Atlas (Lokhorst, 1998), and main roads and towns (33UTM-WGS84 projection). For orientation, an overview map shows the distribution of Rotliegend sediments (grey shaded) and the location of the study area (stippled rectangle). **NWGB** Northwest German Basin, **NEGB** Northeast German Basin, **PT** Polish Trough.

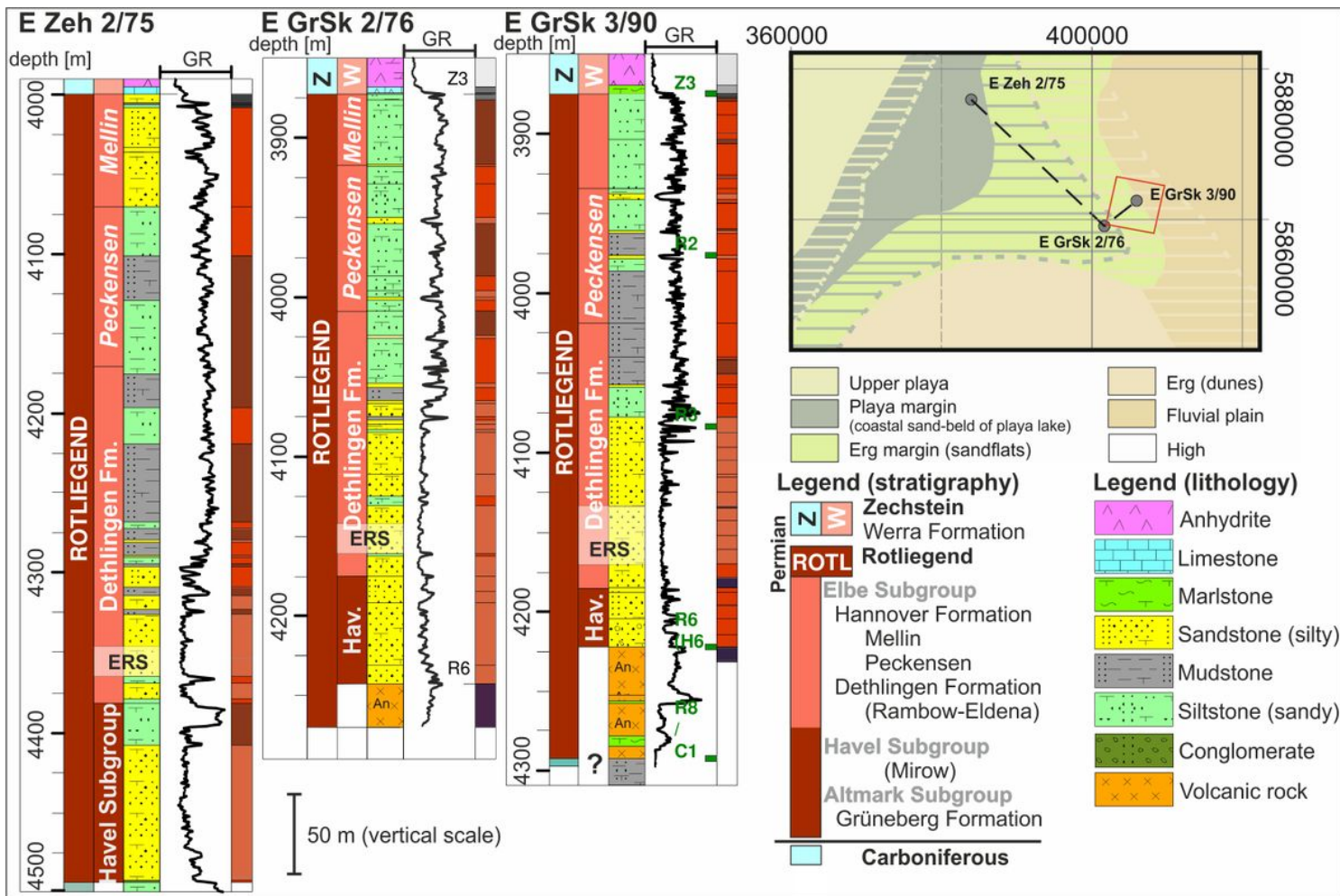


Figure 2

The Rotliegend in East Brandenburg (Groß Schönebeck) as encountered in selected boreholes and respective facies interpretation according to Doornenbal et al. (2010; inset map). ERS marks the sedimentary geothermal target (Elbe reservoir sandstone).

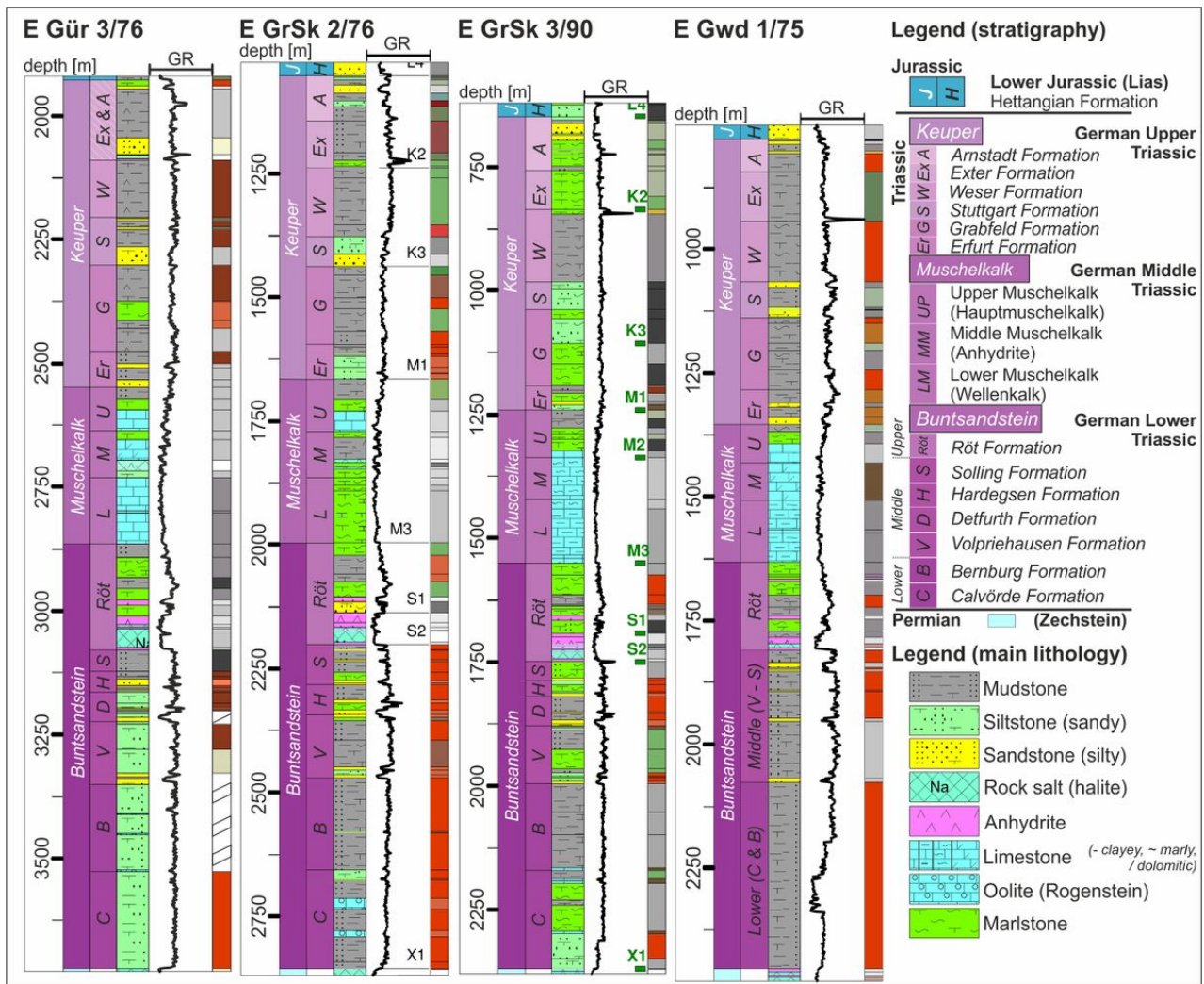


Figure 3
 German Triassic deposits (thickness, lithological composition, and prevailing rock colour) as encountered in boreholes in East Brandenburg from drilling reports. For location of boreholes, see Fig. 1.

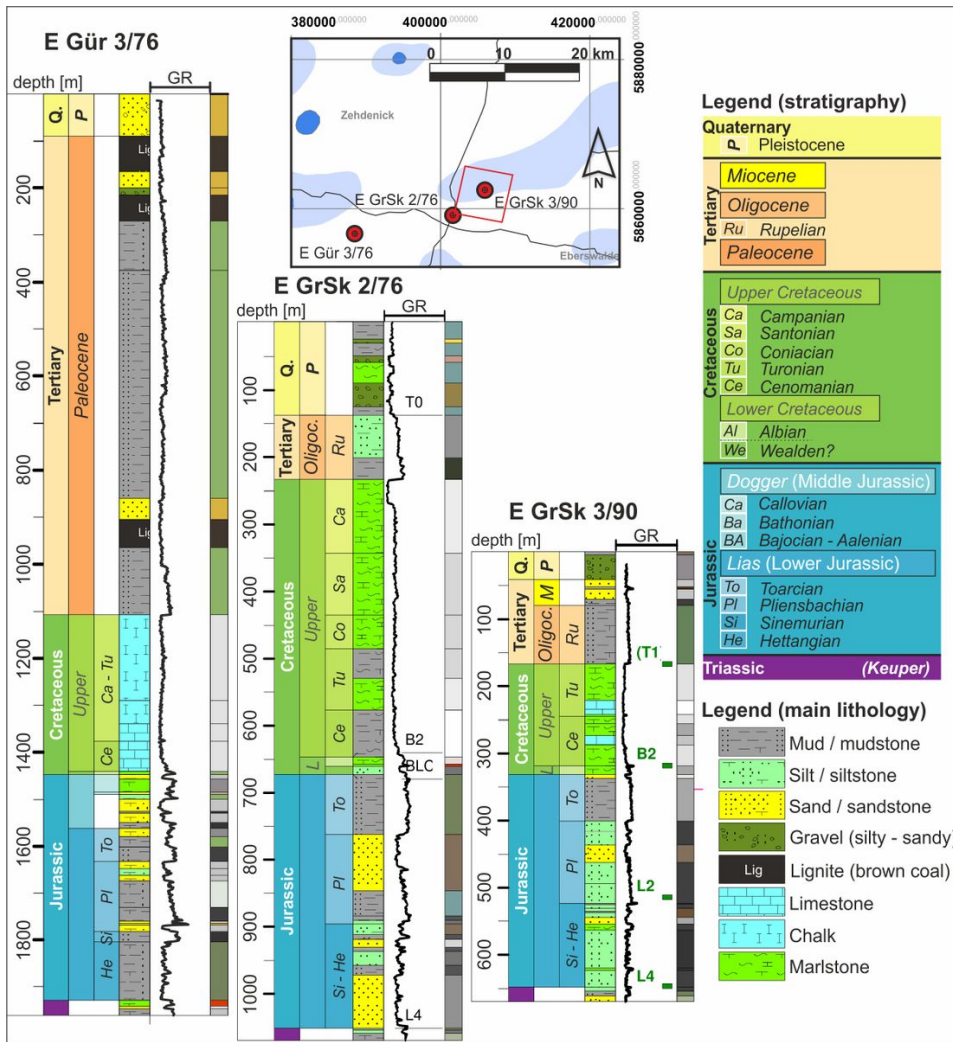


Figure 4
 Jurassic, Cretaceous and Cenozoic deposits (thickness, main lithological composition and prevailing rock colour) as encountered in the Grüneberg (E Gür 3/76) and Groß Schönebeck (E GrSk 2/76, E GrSk 3/90) boreholes in East Brandenburg (from drilling reports).

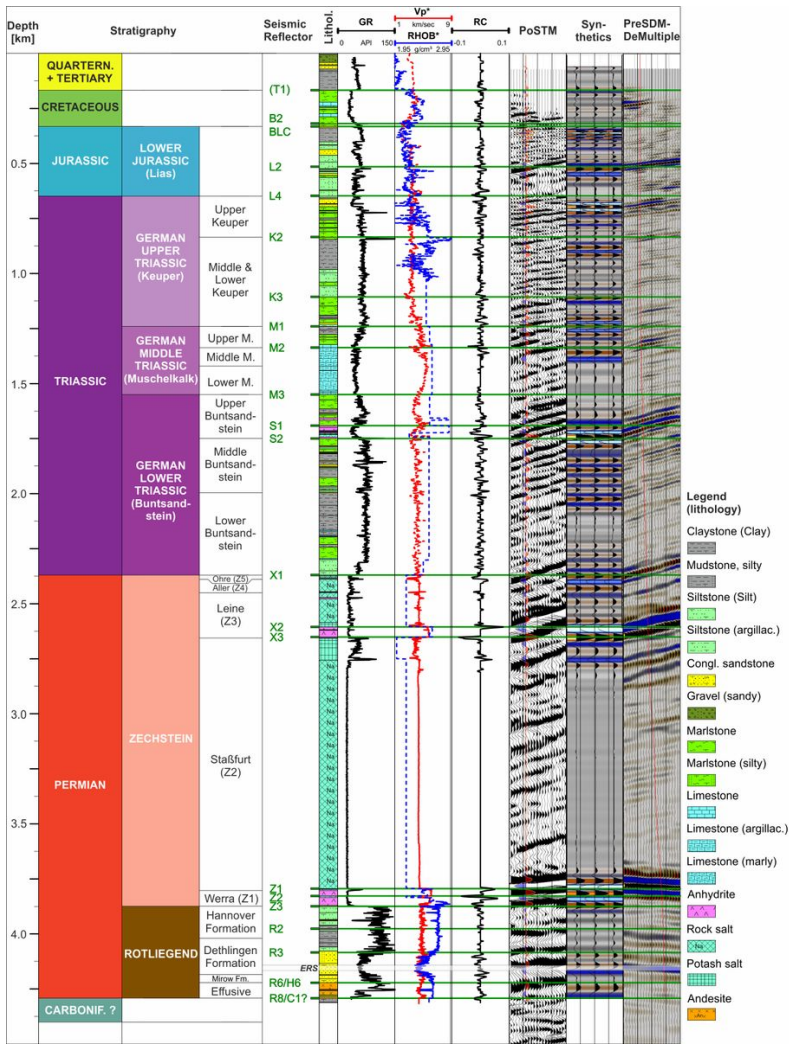


Figure 5

Seismic-well tie of borehole data (E GrSk 3/90 borehole) and seismic volumes. V_p^* refers to sonic velocity (in kms^{-1}), RHOB^* to bulk density logging (in 10^{-3}kgm^{-3} or gcm^{-3}), and RC represents the reflector coefficient, ERS: Elbe reservoir sandstone. The synthetic seismic response based on the applied wavelet is shown together with two processed seismic volumes: PoSTM (post-stack time migration) and PreSDM (pre-stack depth migration with suppression of seismic multiples). Stippled lines of the sonic-density composite plot (V_p^* , RHOB^*) indicate interpolated log responses, see text.

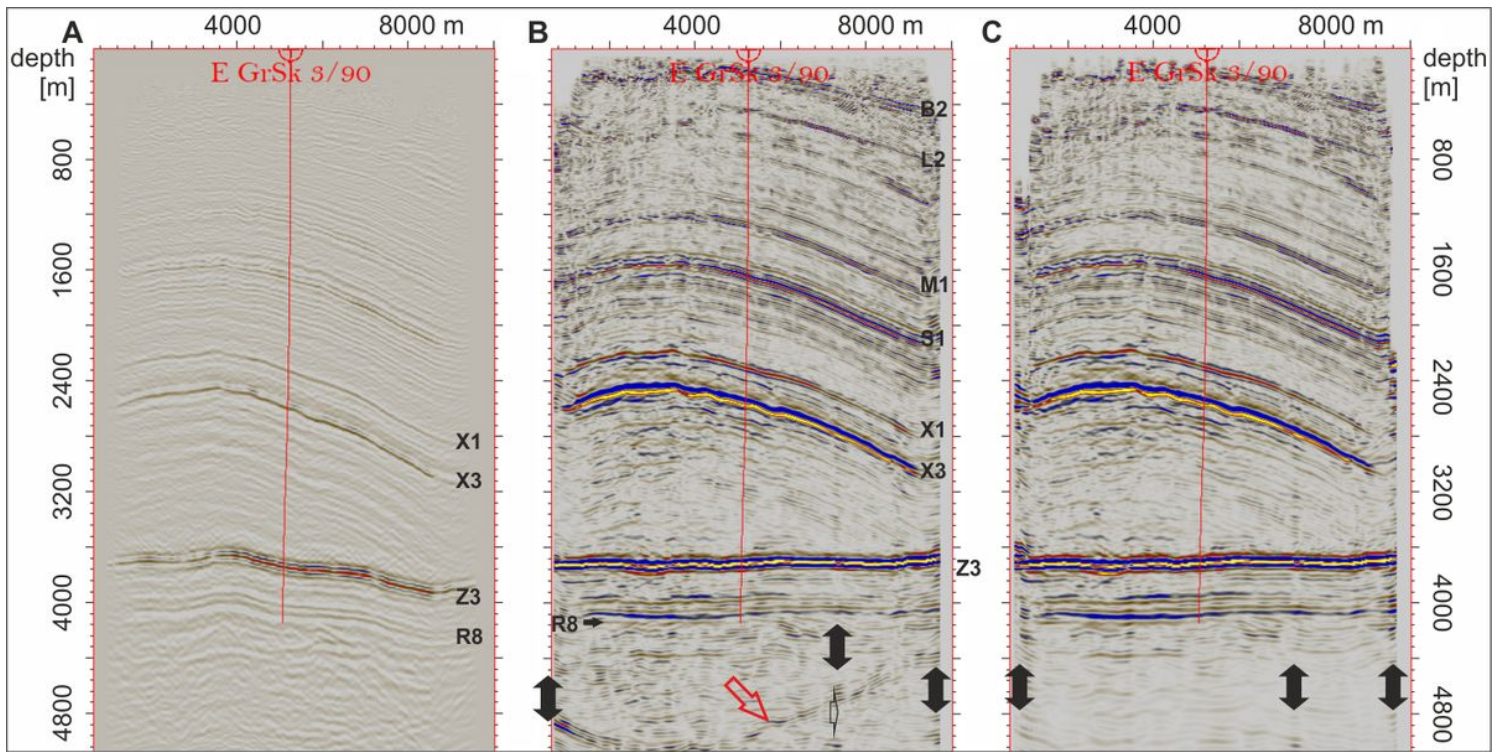


Figure 6

Seismic sections along NW-SE trending profile B (for location see Fig. 7). A: Depth-converted post-stack time migration without CRS stack, B: Pre-stack depth migration with CRS stack after dephasing, C: Pre-stack depth migration with multiple reduction after dephasing (see also Table 1). Black arrows indicate processing artefacts; the red arrow marks a multiple reflection.

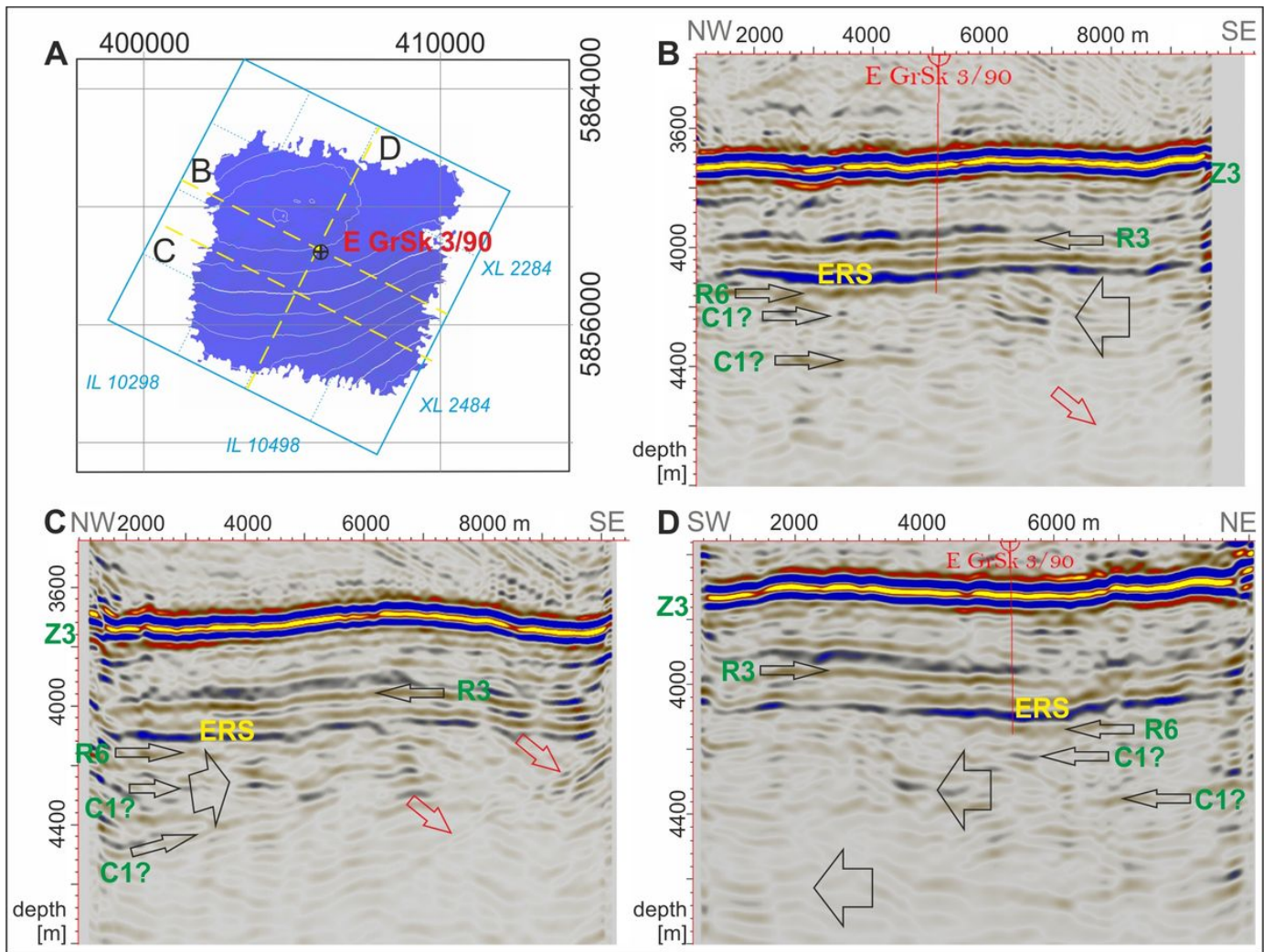


Figure 7
 Seismic cross sections imaging the Rotliegend and pre-Permian at the Groß-Schönebeck site. A: locations of the profiles presented and borehole E GrSk 3/90. B and C: NW-SE sections, D: NNE-SSW section. The base of the Zechstein salt is evident by the dominant reflector band in all three sections (the lowermost interpreted as Z3). Mainly homogeneous internal reflections within the Rotliegend successions are prevailing (R3, R6, C1), and the Elbe reservoir sandstone (ERS) could be recognized as continuous reflection band. Several internal features occur in the pre-Rotliegend below the base of the Havel Subgroup (R6, black arrows). The red arrows mark seismic multiples.

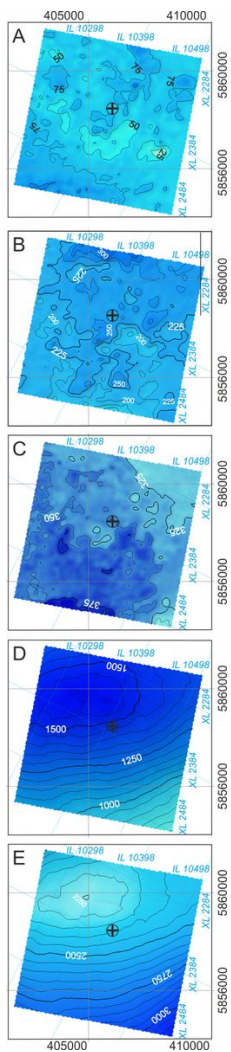


Figure 8

Thickness maps determined from the 3D seismic data in Groß-Schönebeck (contour lines are given in metres; see text for detail). Two alternative interpretations of the Permo-Carboniferous volcanic succession are given, following the reflection found at the formerly hypothesized thickness of ca. 70 m (A) and the interpretation of the here introduced C1 reflector (B). C: Sedimentary Rotliegend, D: Zechstein, E: Post-Permian succession. The cross marks the Groß Schönebeck drill site (E GrSk 3/90).

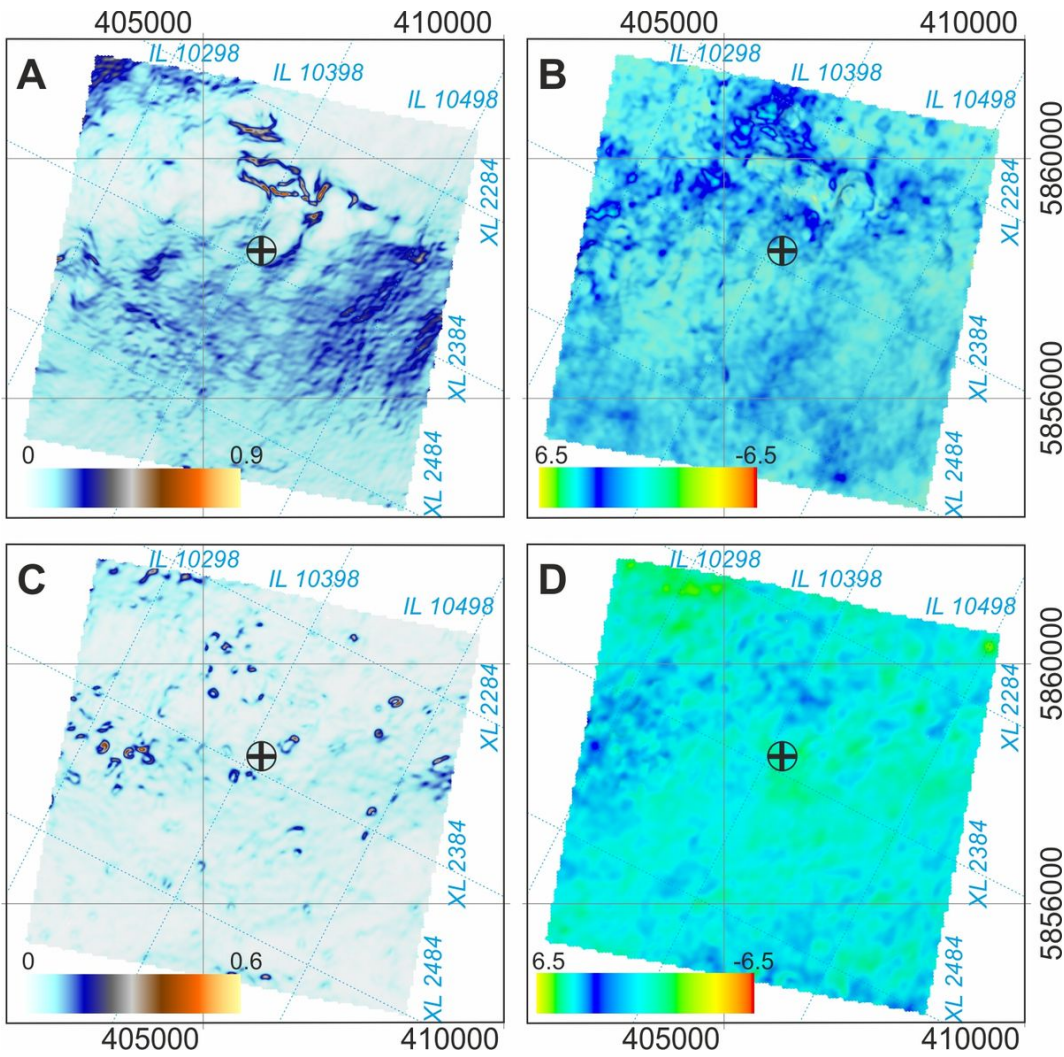


Figure 9
 Seismic attribute analysis applied for fault detection. Left column: variance along interpreted horizons based on CRS volume in time (A: X3 horizon, C: Z3 horizon). Right column: maximum amplitude based on CRS volume in depth (B: X3 horizon, D: Z3 horizon). The graben-like structure within the Leine anhydrite (X3, A and B) is clearly visible while fault signatures are nearly absent at the base of the Zechstein (Z3, C and D). The cross marks the Groß Schönebeck drill site (E GrSk 3/90).

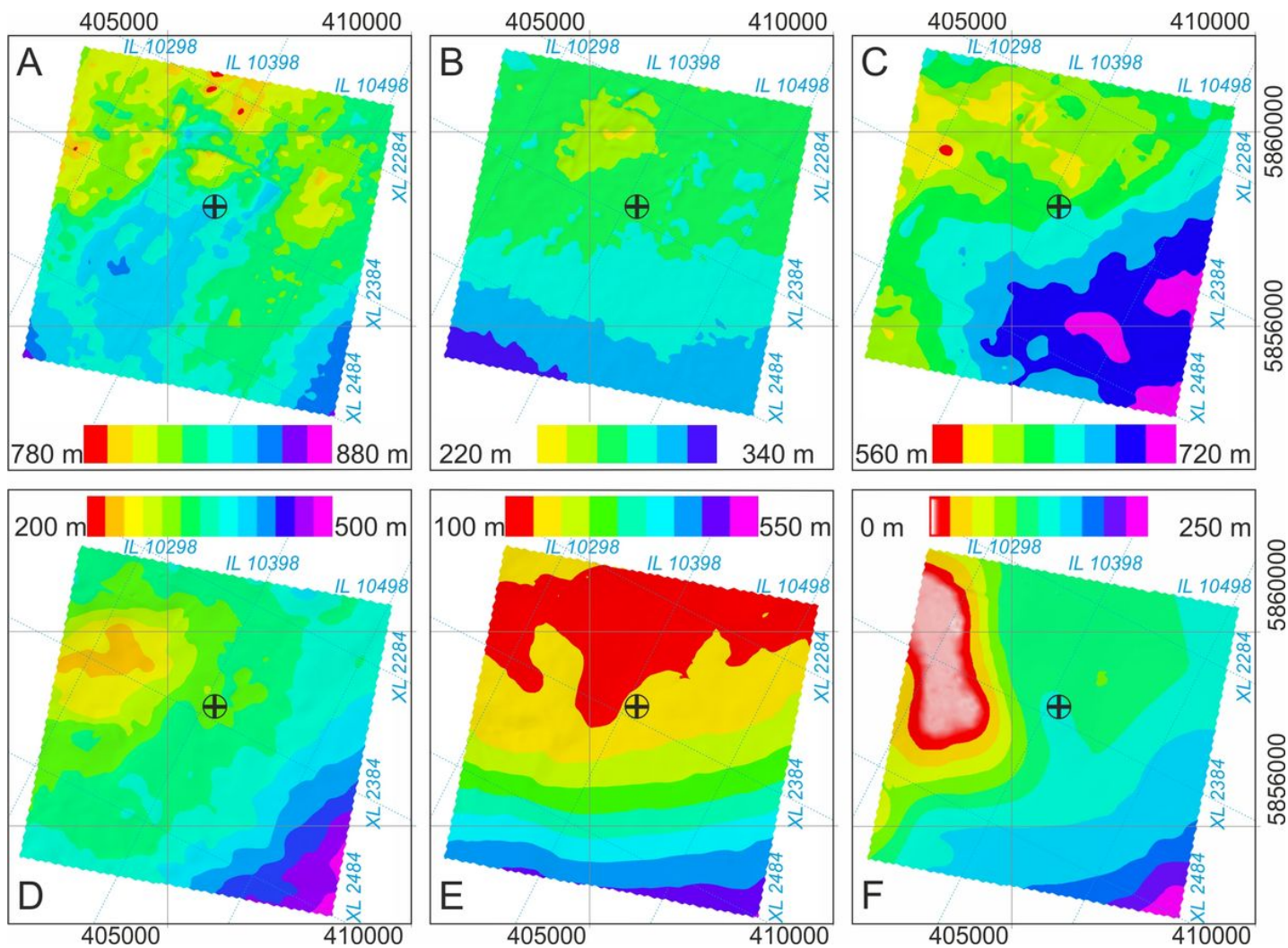


Figure 10

Mesozoic and Tertiary thickness maps. **A** Buntsandstein (M3 – X1), **B** Muschelkalk (M1 – M3), **C** Keuper (L4 – M1), **D** Jurassic (BLC – L4), **E** Cretaceous (based on Stackebrand & Manhenke (2010) and the mapped BLC horizon), **F** Tertiary (mainly based on Stackebrand & Manhenke (2010), combined with borehole data). The cross marks the location of the E GrSk 3/90 borehole.

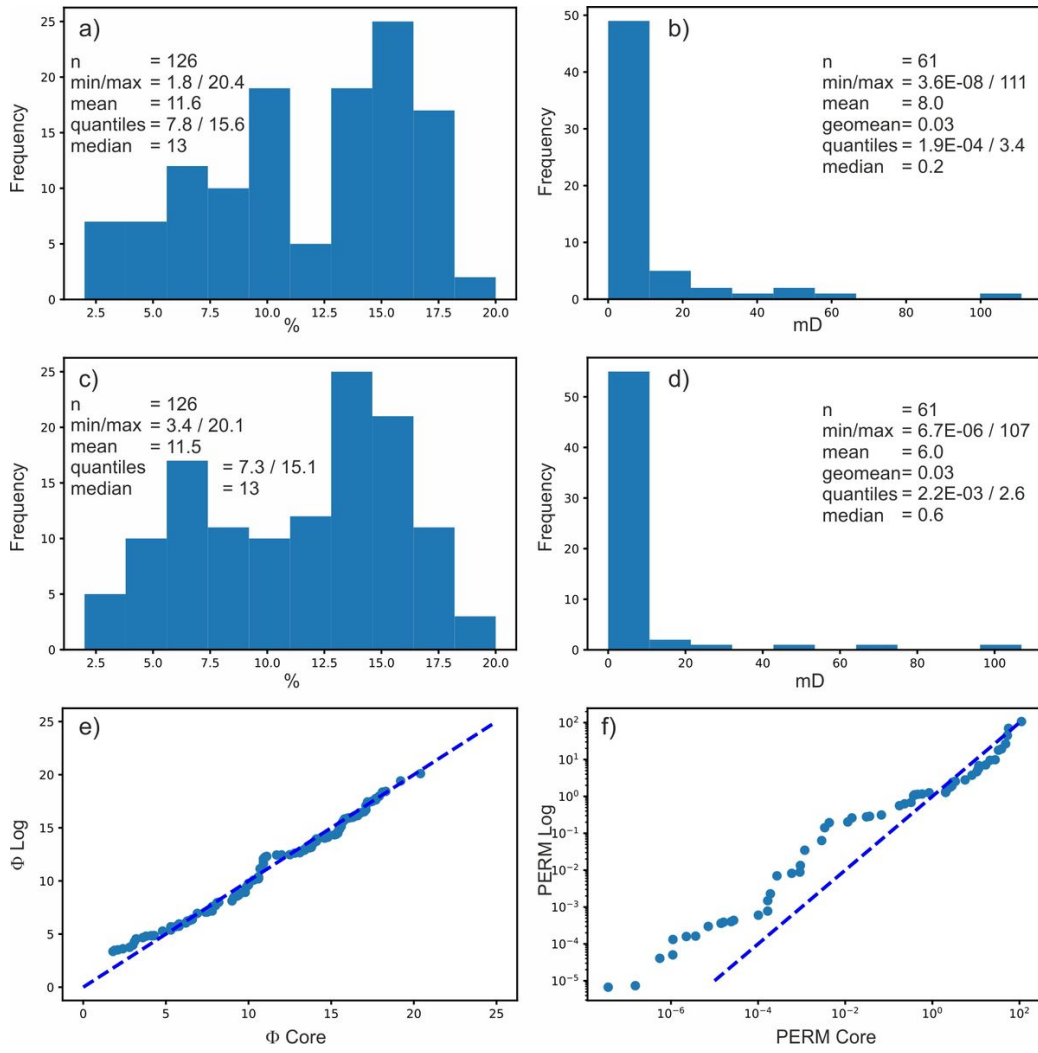


Figure 12

Histograms (a-d) and quantile-quantile plots (e-f) of total porosity (in %) and permeability (in mD) for core data and corresponding log-based data for the stream floodplain facies of the EBS (E GrSk 3/90).

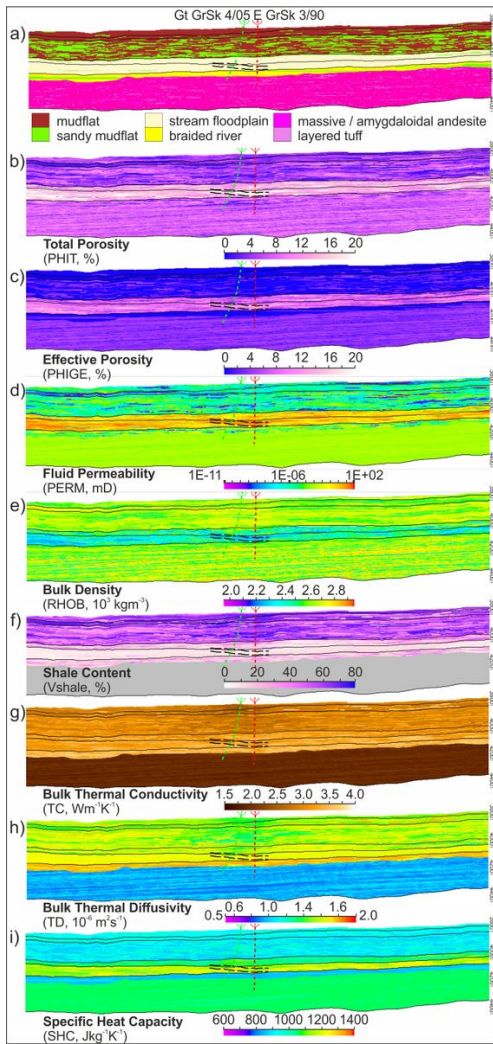


Figure 13

Facies (a) and petrophysical parameterization (b-i), assuming a thickness of the volcanic sequence of about 200 m. Shown are 6.5 km long W-E cross sections covering the central part of the seismic survey in the depth range of 3800 – 4400 m, located approximately 75 – 200 m north to the Groß Schönebeck boreholes (views from the south). Exaggeration: approximately 1.5.

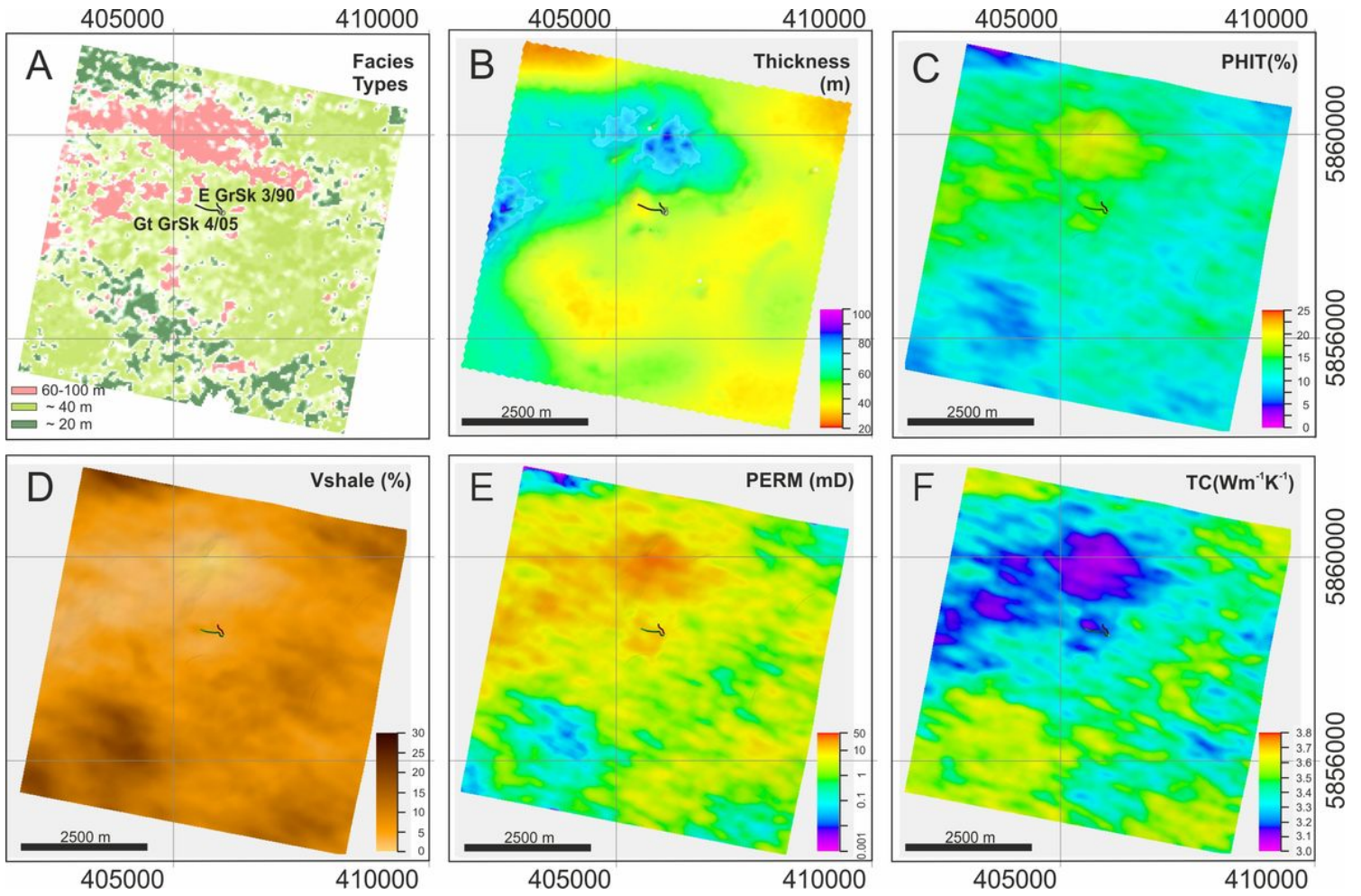


Figure 14

Analysis of the Elbe reservoir sandstone (ERS) derived from reservoir and seismic modelling. A. Seismic facies types in the EBS according to Bauer et al. (2020), B. Thickness map of the EBS (unit 3 in the geological model). Average property maps of the EBS showing total porosity (PHIT, C), shale content (Vshale, D), permeability (mD, E), and thermal conductivity (TC, F). Superimposed are the borehole paths of the GrSk boreholes (black lines in panel centres).

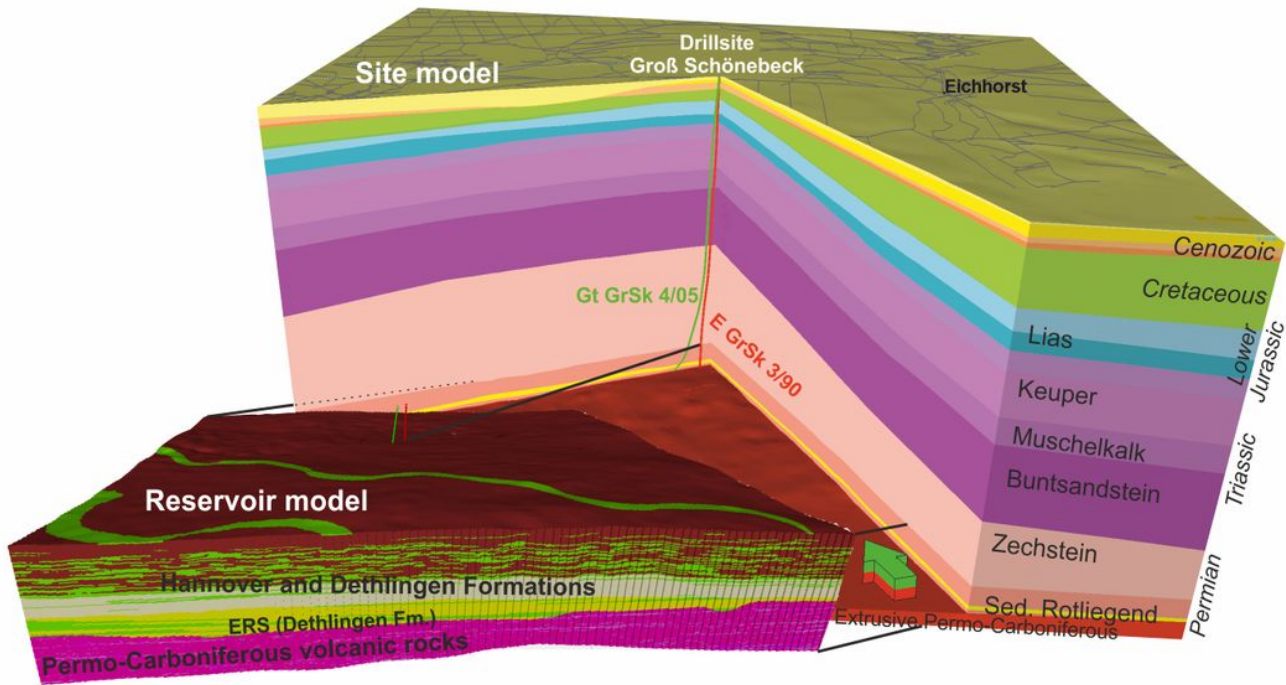


Figure 15

Block visualizations of the new site and reservoir models of the Groß Schönebeck research platform, view from south. The size of the site model is 10 km x 10 km, the size of the reservoir model 6.5 km x 6.5 km.

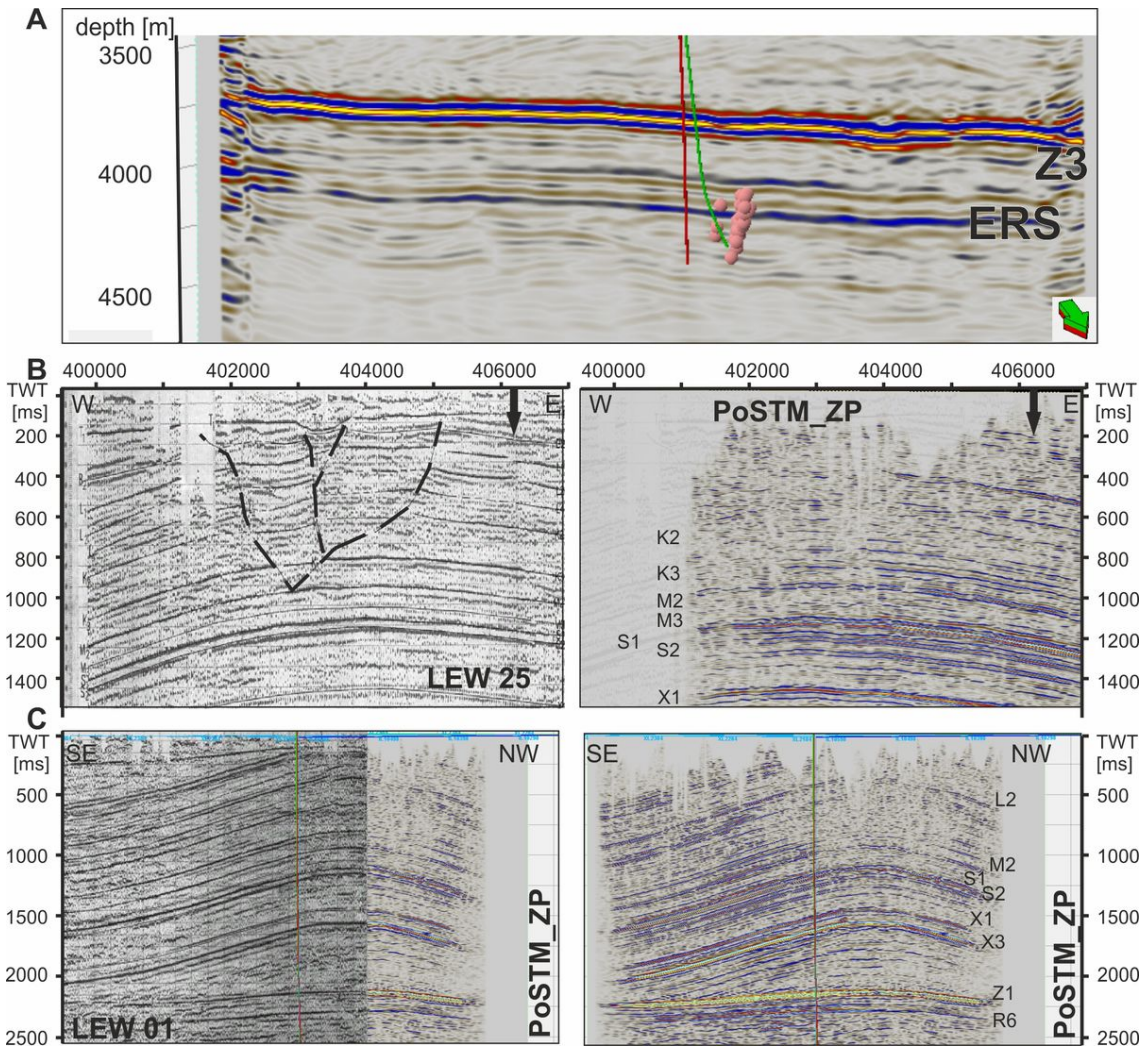


Figure 16

Examples of the high-resolution imaging achieved by the 3D seismics (Krawczyk et al., 2019) in direct comparison with former investigations. A shows the micro-seismic events registered during fluid injection (Kwiattek et al., 2010) superimposed on a cross-section cut from the 3D seismics (Xline 2385, view from south), B and C show the 2D legacy lines LEW25 (view from south) and LEW 1 (view from northeast) on the left-hand side, respectively (courtesy Neptune Energy). For comparison, the corresponding sections cut from the new 3D seismics is shown on the right. The arrow marks the projected drill site of Groß Schönebeck. Stippled lines show former fault interpretations.

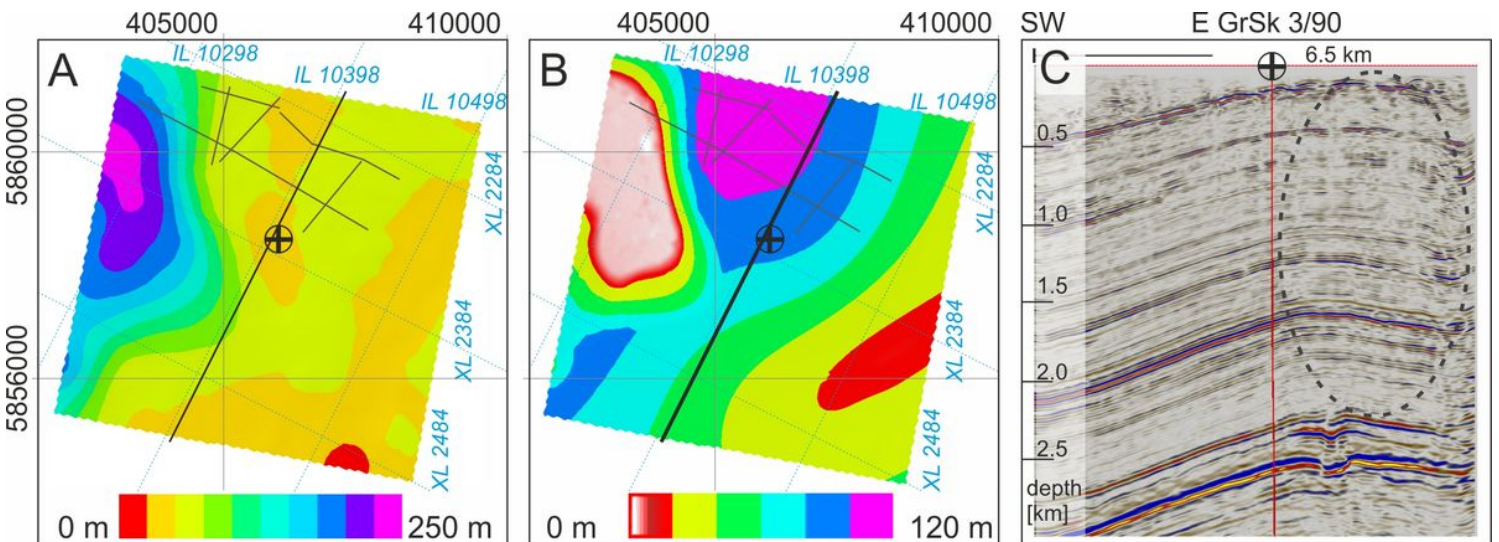


Figure 17

Thickness maps of the Quaternary deposits (A) and of the Tertiary Rupelton (B) based on Stackebrand & Manhenke (2010). Superimposed in grey lines are the mapped main faults in the upper Zechstein (this study) and the orientation of the seismic profile shown in C. C: Seismic section of the pre-stack depth migration volume with CRS stack after depthing (profile D in Figure 6) showing less continuity of seismic reflectors in the stippled area.